# Dendritic NMDA receptors in parvalbumin neurons enable strong and stable neuronal assemblies

Jonathan Cornford[1*], Marion S Mercier[1*], Marco Leite[1], Vincent Magloire[1], Michael Häusser[2], Dimitri M Kullmann[1]

**Affiliations:**

[1]UCL Institute of Neurology, University College London,

[2]Wolfson Institute for Biomedical Research, University College London,

*These authors contributed equally

Correspondence to: jonathan.cornford@gmail.com or d.kullmann@ucl.ac.uk

**Abstract**: Parvalbumin-expressing (PV+) GABAergic interneurons mediate feedforward and feedback inhibition and have a key role in gamma oscillations and information processing. The importance of fast synaptic recruitment, action potential initiation and repolarization, and rapid synchronous GABA release by PV+ cells is well established. In contrast, the functional significance of PV+ cell NMDA receptors (NMDARs), which generate relatively slow postsynaptic currents, is unclear. Underlining their importance, several studies implicate PV+ cell NMDAR disruption in impaired network function and circuit pathologies. Here, we show that dendritic NMDARs underlie supralinear integration of feedback excitation from local pyramidal neurons onto mouse CA1 PV+ cells. Furthermore, by incorporating NMDARs at feedback connections onto PV+ cells in spiking networks, we show that these receptors enable cooperative recruitment of PV+ interneurons, strengthening and stabilising principal cell assemblies. Failure of this phenomenon provides a parsimonious explanation for cognitive and sensory gating deficits in pathologies with impaired PV+ NMDAR signalling.

## Introduction

Interactions among cell assemblies underlie information representation and processing in the brain (Buzsáki, 2010). Inhibitory interneurons, including fast-spiking PV+ cells, which mediate feedforward and feedback inhibition and are central to gamma oscillations, have a major role in segregating excitatory principal cells into functional groups. PV+ cells have broad receptive fields inherited from multiple converging heterogeneously tuned principal neurons (Kerlin et al., 2010) and coupled with their powerful somatic inhibition of principal cells, they are positioned to mediate a 'winner-takes-all' scheme in which neuronal assemblies inhibit each other (Agetsuma et al., 2018; Trouche et al., 2016).

The biophysical properties of PV+ cells that make them suited to fast inhibition of target neurons are well established (Jonas et al., 2004). These properties are critical for functions such as the enforcement of narrow temporal integration, input normalization, and sparsification of neuronal assemblies (de Almeida et al., 2009; Pouille et al., 2009; Pouille and Scanziani, 2001). However, PV+ interneurons are also equipped with NMDARs whose slow kinetics and nonlinear voltage dependence do not appear well-aligned with fast inhibition of principal cells. Although NMDARs contribute relatively less to synaptic excitation of PV+ cells than principal neurons (Geiger et al., 1997; Lamsa et al., 2007; Matta et al., 2013), several sources of evidence suggest that they are important for the normal operation of cell assemblies. In particular, genetic deletion of NMDARs in PV+ interneurons disrupts both gamma rhythms (Carlén et al., 2012) and spatial representations (Korotkova et al., 2010). Moreover, impaired NMDAR-mediated signalling in PV+ interneurons has been suggested to be a core feature of schizophrenia (Coyle, 2012; Lisman et al., 2008). Indeed, genetic manipulation of the schizophrenia risk genes encoding neuregulin and ErbB4, which amongst other functions regulate NMDARs, impairs recruitment of PV+ interneurons and recapitulates some features of the disease (delPino et al., 2013; Kotzadimitriou et al., 2018).

A recent study investigating plasticity rules of glutamatergic inputs onto CA1 PV+ interneurons reported NMDAR-dependent long-term potentiation (LTP) at feedback synapses from local pyramidal neurons but not at feedforward connections made by Schaffer collaterals (Le Roux et al., 2013), and attributed the difference to a larger NMDAR conductance at feedback synapses. A natural question prompted by these findings is the degree to which NMDARs contribute towards synaptic integration of glutamatergic feedback inputs on PV+ cells. In principal neurons, NMDAR-mediated dendritic nonlinearities enhance the computing capacity of individual cells (Gasparini, 2006; Losonczy and Magee, 2006; Poirazi and Mel, 2001; Stuart and Spruston, 2015). Do NMDARs have an analogous function in PV+ interneurons? Furthermore, given the importance of excitatory feedback connections on interneurons for microcircuit motifs, how do NMDARs in PV+ interneurons affect interactions between neuronal assemblies?

Here we combine *in vitro* optogenetic stimulation and two-photon glutamate uncaging with modelling to assess the role of NMDARs at excitatory feedback connections onto mouse hippocampal CA1 PV+ interneurons. We show that NMDARs at feedback synapses mediate integrative dendritic nonlinearities in PV+ interneurons. Importantly, this mechanism can be exploited to promote the formation of robust cell assemblies that are stable in the face of distracting noise.

## Results

### Differential input integration at stratum oriens and stratum radiatum dendrites of PV+ interneurons.

Experiments were performed in acute hippocampal slices from mice obtained by crossing PV-Cre mice with Ai9 mice, and tdTomato expression was used to target fast-spiking PV+ interneurons in CA1 stratum pyramidale. Such neurons, which mainly comprise basket cells in addition to axo-axonic and bistratified cells (Bezaire and Soltesz, 2013), receive excitatory feedforward inputs across the full extent of their dendritic trees, in both strata radiatum and oriens. In contrast, feedback inputs from axon collaterals of local pyramidal cells are confined to dendrites in the stratum oriens (Amaral et al., 1991). In order to compare the contribution of NMDARs to dendritic integration of feedforward and feedback excitatory postsynaptic potentials (EPSPs), we took advantage of the anatomical restriction of feedback inputs onto oriens dendrites, and recorded somatic responses to two-photon glutamate uncaging at multiple sites within a 15 µm dendritic segment in either stratum oriens or stratum radiatum (**Figure 1A**). Activation of individual uncaging locations in either stratum evoked uncaging-evoked EPSPs (uEPSPs) that were comparable in amplitude and kinetics to spontaneous EPSPs (**Figure 1B** and Figure 1 – Figure Supplement 1), consistent with a high density of excitatory synapses innervating PV+ interneuron dendrites (Gulyás et al., 1999). To quantify the degree of nonlinearity of dendritic integration, we compared compound uEPSPs elicited by near-synchronous activation of increasing numbers of uncaging locations to the arithmetic sum of individual uEPSPs at the same sites (**Figure 1C**). Activation of sites on dendrites in stratum oriens revealed supralinear uEPSP summation (peak amplitude nonlinearity: 24.0 ± 4.5%, mean ± SEM, n = 14; **Figure 1D,E**; unscaled responses in Figure 1 – Figure Supplement 2). This nonlinearity was even larger when measured using the time-integral of uEPSPs measured between 0 and 50 ms from onset (time-integral nonlinearity: 54.0 ± 10.1%; **Figure 1F**). In contrast, when glutamate was uncaged along dendritic segments in stratum radiatum, uEPSPs summated in an approximately linear fashion (peak amplitude nonlinearity: 3.8 ± 5.0%, time-integral nonlinearity: 6.3 ± 7.6%, n = 9; oriens vs. radiatum $P = 0.0083$ and $P = 0.0028$ for peak amplitude and time-integral comparisons respectively, unpaired *t*-tests, **Figure 1D–F**). The difference between strata was also observed in a subset of paired recordings in which dendrites in both strata were tested (Figure 1 – Figure Supplement 3). There was no significant relationship between integration nonlinearity and either uncaging distance from soma or the size of the arithmetic sum of the uEPSPs (Figure 1 – Figure Supplement 4). Given that synapses in stratum oriens are innervated by both local pyramidal neurons and Schaffer collaterals, the striking supralinear summation of uEPSPs uncovered here may underestimate the true extent of dendritic nonlinearity at feedback connections.

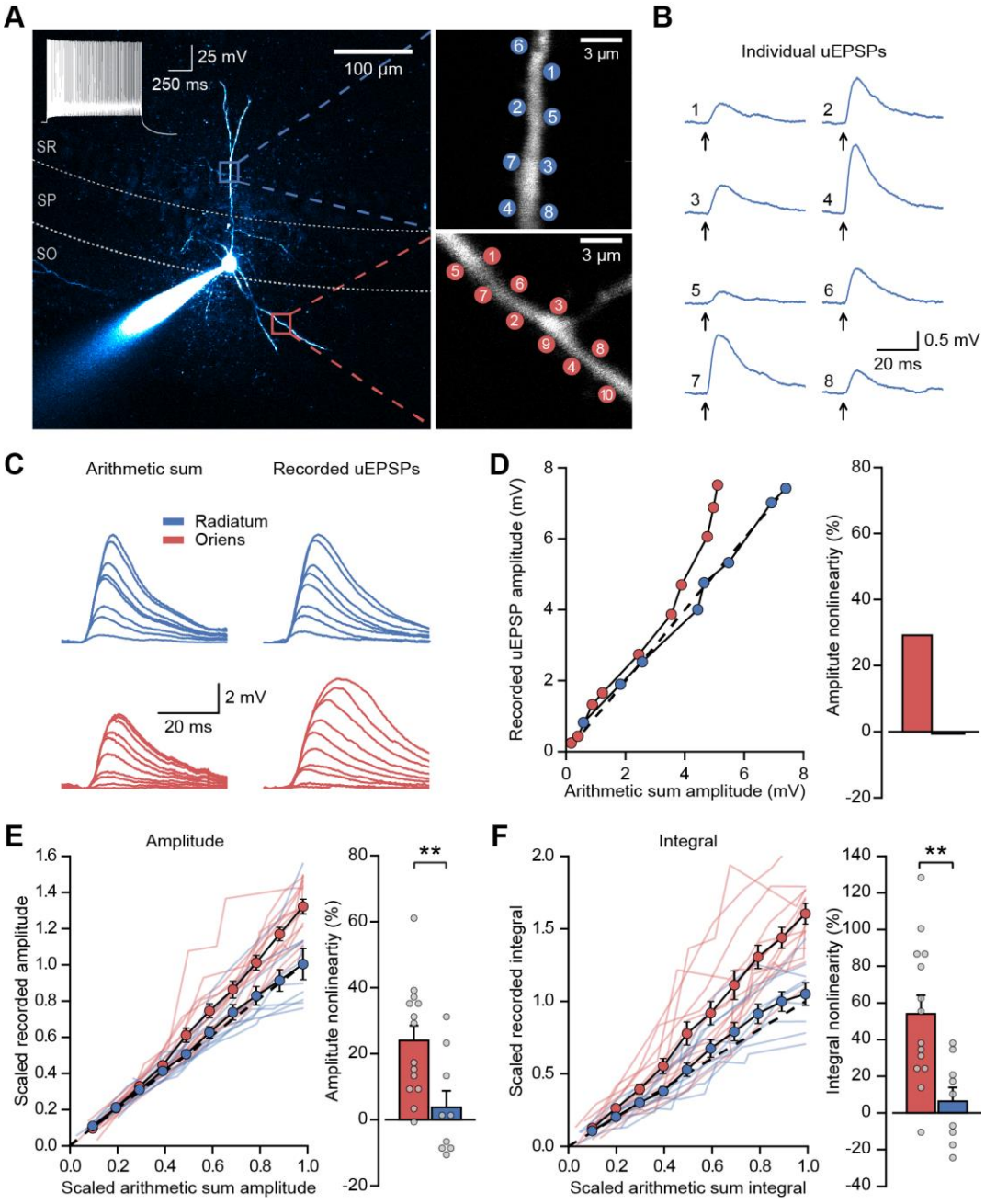


**Figure 1. Differential input integration at stratum oriens and stratum radiatum dendrites of PV+ interneurons.**

(**A**) Two-photon z-projection image of a PV+ interneuron recorded via a patch pipette in stratum pyramidale (SP) and filled with Alexa-594 (left), with two dendritic regions of interest at higher magnification (right: top, stratum radiatum, SR; bottom, stratum oriens, SO), showing glutamate uncaging locations (numbered).

(**B**) Individual uEPSP responses from radiatum dendritic locations shown in (A).

(**C**) Comparison of arithmetic sum of individual uEPSPs and recorded uEPSPs evoked by near-synchronous uncaging at multiple locations in stratum radiatum (blue) and oriens (red).

(**D**) Peak amplitudes of recorded uEPSPs plotted against arithmetically summed waveforms for the two regions shown in (A). Dashed line shows line of identity. Right: bar chart showing percentage amplitude nonlinearity. Red: oriens, blue: radiatum.
(**E**) Summary of scaled peak amplitude comparisons for all cells (oriens locations: n = 14, radiatum locations: n = 9). Filled circles and error bars indicate mean ± SEM. Right: bar chart showing quantification of amplitude nonlinearity.
(**F**) Time-integral nonlinearity plotted as for (E). **: $p < 0.01$.

We repeated these experiments with uncaging locations distributed across two dendrites in stratum oriens, and compared the degree of non-linearity to that observed when uncaging was confined to either one of the dendrites. The degree of supralinear summation was significantly lower when uncaging was distributed across two dendrites (peak amplitude nonlinearity, 39.3 ± 11.7 % vs 16.5 ± 5.6 %, $P = 0.016$, n = 12; paired *t*-test; Figure 1 – Figure Supplement 5). This result implies that the spatial clustering, or conversely dispersion, of co-active dendritic inputs to PV+ interneurons has an important role in input integration.

**NMDAR expression and dendrite morphology underlie stratum-dependent differences in synaptic integration.**

Supralinear dendritic integration in pyramidal neurons depends on the recruitment of voltage-dependent conductances. We therefore investigated the role of such conductances in PV+ interneurons. In line with previous evidence for a substantial NMDAR component at feedback inputs onto PV+ cells (Le Roux et al., 2013), supralinear dendritic summation in stratum oriens was abolished when NMDARs were blocked by D-AP5 (100 µM) (time-integral nonlinearity: 2.5 ± 3.0 %, vs control without the drug $P = 0.0004$, n = 10; **Figure 2A–C**). Dendritic integration in stratum radiatum was unchanged from control conditions (time-integral nonlinearity: 3.3 ± 2.6 %, vs control $P = 0.88$, n = 4; **Figure 2A–C**). In contrast to D-AP5, the sodium channel blocker tetrodotoxin (TTX, 100 nM) did not significantly affect integration in either stratum oriens or radiatum (oriens time-integral nonlinearity 40.1 ± 5.6 %, vs control $P = 0.23$, n = 16; radiatum time-integral nonlinearity 9.4 ± 3.3 %, vs control $P = 0.71$, n = 9; **Figure 2D**). The failure of TTX to affect uEPSP integration is consistent with the view that PV+ interneuron dendrites generally do not support regenerative events (Hu et al., 2010) (although see (Chiovini et al., 2014)). The effects of pharmacological manipulations were consistent whether measuring time-integrals or peak uEPSP amplitudes (Figure 2 – Figure Supplement 1). Furthermore, uncaging distances from soma were comparable across all conditions, as were somatic uEPSP amplitudes (Figure 2 – Figure Supplement 2). Dendrites of PV+ interneurons that mediate feedback inhibition, but not those mediating purely feedforward inhibition, thus exhibit NMDAR-dependent supralinear input integration. These

findings imply that clusters of coactive synapses supplied by local pyramidal neurons cooperate via depolarization-dependent relief of NMDARs from $Mg^{2+}$ blockade.

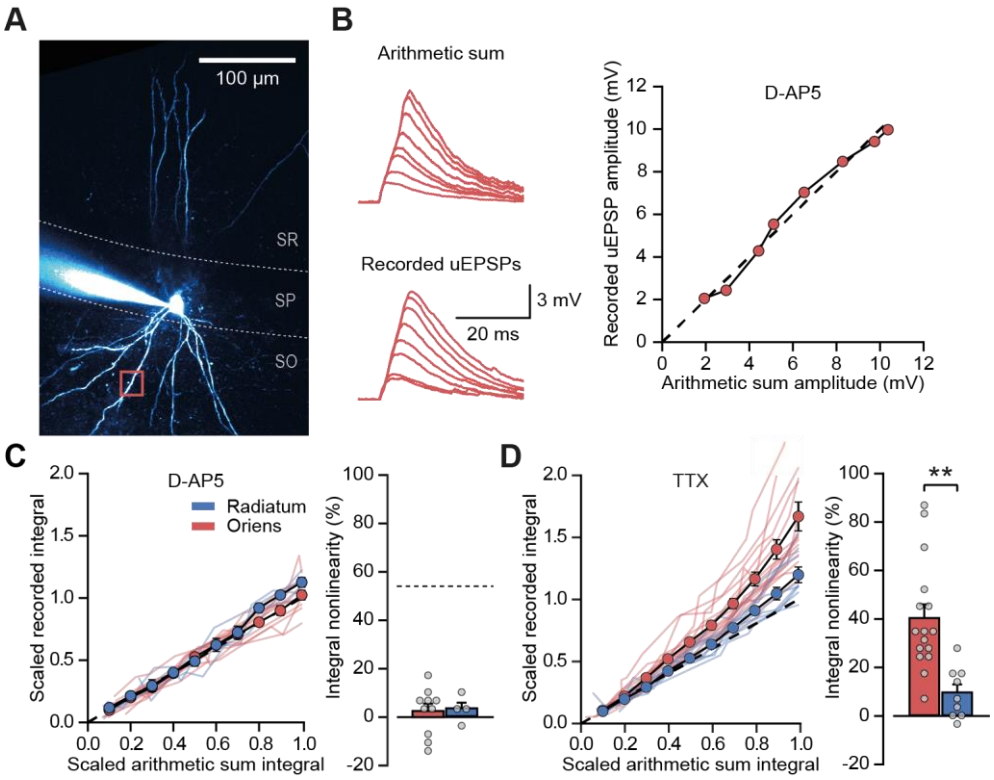


**Figure 2. NMDARs mediate stratum oriens dendrite synaptic integration supralinearity.**
(**A**) Two-photon z-stack of PV+ interneuron in CA1 region of hippocampus. Red box marks glutamate uncaging location.
(**B**) Comparison of arithmetic and recorded uEPSP summation waveforms in the presence of D-AP5. Right: peak recorded amplitude vs peak arithmetic amplitude.
(**C**) Summary data of time-integrals plotted against arithmetic sum time-integrals for 14 dendritic locations recorded in D-AP5 (oriens locations: n = 10, radiatum locations: n = 4). Right: quantified synaptic integration nonlinearity. The dashed line marks the average magnitude of oriens nonlinearity from Figure 1F.
(**D**) Summary data for 25 dendritic locations recorded in TTX (oriens locations: n = 16, radiatum locations: n = 9). Right: quantification of synaptic integration nonlinearity. Filled circles and error bars indicate mean ± SEM.

The results above are consistent with previous evidence of a larger NMDAR/AMPAR conductance ratio at feedback than feedforward synapses, estimated by electrically stimulating axons in the alveus/stratum oriens or stratum radiatum respectively, while clamping PV+ interneurons at positive and negative potentials to separate AMPAR

and NMDAR components (Le Roux et al., 2013; Pouille and Scanziani, 2004). However, the low input resistance of PV+ interneurons, together with different dendritic morphologies in strata oriens and radiatum (Hu et al., 2010), potentially confounds the comparison of excitatory postsynaptic currents (EPSCs) originating from the two locations and recorded at positive holding potentials (Williams and Mitchell, 2008). We therefore used an alternative experimental design to estimate the relative contribution of AMPARs and NMDARs. Specifically, we recorded EPSCs in a low (0.1 mM) extracellular [$Mg^{2+}$] solution to partially unblock NMDARs while holding PV+ interneurons at –60 mV, and used sequential addition of AMPAR and NMDAR blockers to separate the two components of transmission (**Figure 3A**).

Pharmacological dissection of EPSCs in 0.1 mM [$Mg^{2+}$] revealed a >2-fold greater NMDAR/AMPAR charge ratio when stimulating in the alveus than when stimulating in stratum radiatum (charge ratio: 3.5 ± 0.7 vs 1.3 ± 0.3, $P = 0.0017$, n = 10, paired *t*-test; **Figure 3A**). The decay time constant of the NMDAR-mediated EPSCs was similar for the two inputs (Schaffer collaterals: 154.6 ± 25.9 ms vs alveus: 148.1 ± 13.4 ms, $P = 0.8$, n = 10, paired *t*-test; **Figure 3B**) providing no evidence for differences in NR2B subunit inclusion, again consistent with previous work that showed similar effects of selective blockade of NR2B-containing receptors (Le Roux et al., 2013) (although see (Matta et al., 2013)).

Dendrites of PV+ interneurons in stratum oriens are generally thinner and shorter than those in stratum radiatum (Gulyás et al., 1999) suggestive of a higher effective local input impedance. This raises the possibility that, in addition to enriched NMDAR expression, oriens dendrites may be depolarized more effectively by glutamate uncaging resulting in an enhanced relief of NMDARs from voltage-dependent $Mg^{2+}$ block (Branco et al., 2010). To investigate the relationship between synaptic integration and dendritic geometry we used a detailed compartmental model of a CA1 PV+ interneuron (**Figure 3C**). Voltage-dependent conductance densities and membrane properties were implemented according to previously published models (Hu and Jonas, 2014; Nörenberg et al., 2010), and the relative densities of synaptic AMPARs and NMDARs were initially assumed to be the same on oriens and radiatum dendrites. Simulation parameters closely followed the uncaging experiments, with clusters of synapses activated across the range of experimentally measured locations. These simulations revealed supralinear summation of EPSPs recorded at the soma that was more pronounced for stratum oriens than for stratum radiatum dendrites (oriens vs radiatum time-integral nonlinearity: 42.5 ± 3.5 % vs 23.9 ± 2.3 %, $P < 0.001$, **Figure 3D**), supporting a role for dendritic morphology in mediating the difference between strata. The simulation results were very similar whether AMPARs were assumed to show polyamine-dependent inward rectification or to have a fixed open-channel conductance (Figure 3 – Figure Supplement 1). The ~ 2-fold difference in supralinearity between strata was, however, smaller than the >8-fold difference observed experimentally (oriens vs radiatum time-integral nonlinearity: 54.0 ± 10.1 % vs 6.3 ± 7.6 %; **Figure 1**).

Reducing the simulated NMDAR/AMPAR conductance ratio at radiatum dendrites to half that of the oriens dendrites, in line with results from experiments in **Figure 3A**, improved agreement with the glutamate uncaging data (time-integral supralinearity in simulations: 42.5 ± 3.5 % vs 8.5 ± 0.8 % for stratum oriens vs stratum radiatum; **Figure 3E**). The difference in dendritic integration in oriens and radiatum dendrites observed experimentally (**Figure 1**) may therefore be accounted for by a combination of differential NMDAR expression (greater in stratum oriens) and dendritic morphology (greater impedance in stratum oriens, thus facilitating depolarization and NMDAR opening).

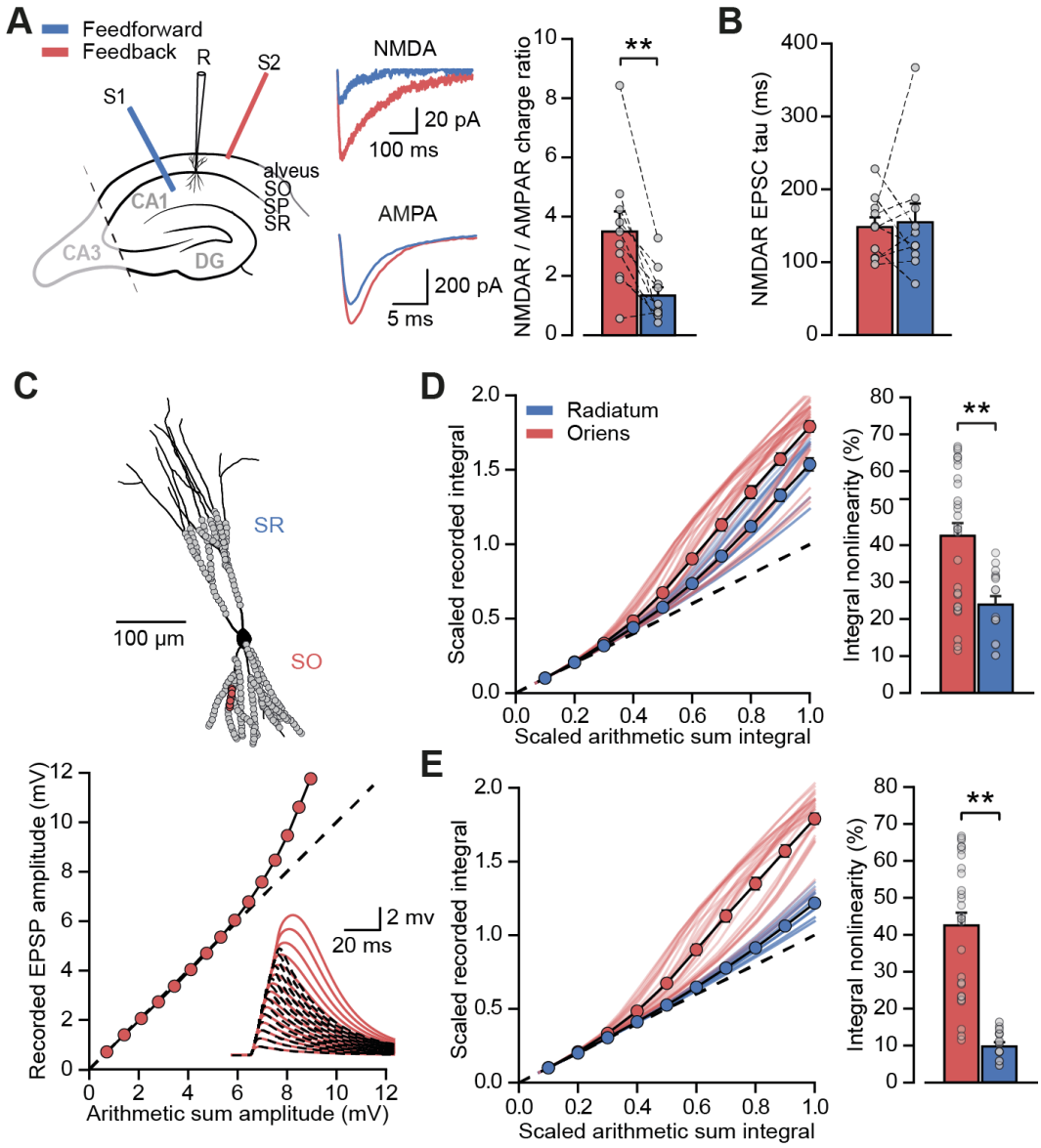


**Figure 3 Differential NMDAR expression and dendrite morphology explain stratum-dependent synaptic integration difference.**

(**A**) Schematic describing stimulation of feedforward (S1, blue) and antidromic stimulation of feedback (S2, red) axons. Middle: example paired AMPAR and NMDAR EPSC components in low [$Mg^{2+}$]. Right: NMDAR/AMPAR charge ratios (n = 10).
(**B**) Decay time constants of NMDAR-mediated EPSCs recorded in the same PV+ neurons in response to stimulation of feedforward (blue) and feedback (red) axons (n = 10).
(**C**) Top: reconstruction of a PV+ interneuron (axon not shown). Simulated synaptic locations are shown in gray. Bottom: example simulated uncaging experiment at the synapses marked with red circles; graph shows recorded EPSP amplitudes vs arithmetic sum of EPSP amplitudes. Inset: red solid lines, recorded summation; dashed black lines, arithmetic summation; waveforms calculated from individual synaptic responses.
(**D**) Scaled recorded time-integrals vs scaled arithmetic sum of time-integrals at all locations with equal NMDAR conductance (oriens locations: n=28, radiatum locations: n=16). Right: quantified synaptic integration nonlinearity.
(**E**) As (D), but with reduced NMDAR/AMPAR conductance ratio at radiatum dendrites. Oriens data replotted from (D).

**NMDAR recruitment at CA1 pyramidal cell feedback connections onto PV+ interneurons.**

While electrical stimulation of the alveus recruits local pyramidal cell axon collaterals, it may also recruit other extrinsic afferents that could contribute to the observed NMDAR currents. In order to isolate the feedback input from CA1 pyramidal cells to PV+ interneurons, and to measure the magnitude of the NMDAR component at these synapses, we combined voltage clamp using a $Cs^{+}$-based pipette solution with optogenetic stimulation of feedback fibers. ChR2 was selectively expressed in CA1 pyramidal cells by injecting an adeno-associated virus (AAV) encoding ChR2-EYFP under the control of the CaMKII promoter in CA1 of the dorsal hippocampus. We routinely verified that expression was confined to CA1 and did not spread to CA3 (**Figure 4A**). Wide-field illumination pulses (1ms) of 470 nm light elicited monophasic EPSCs, in agreement with the low associative connectivity among CA1 pyramidal neurons (Amaral et al., 1991; Deuchars and Thomson, 1996) (**Figure 4B**). AMPAR- and NMDAR-mediated light-evoked feedback EPSCs were recorded at -60 mV and +60 mV, respectively, and NBQX was added to isolate the NMDAR component (**Figure 4B**). This revealed large NMDAR currents (amplitude: 459.1 ± 89.2 pA, integral: 39.1 ± 6.8 nA ms) and NMDAR/AMPAR ratios (amplitude: 0.7 ± 0.2, integral: 2.7 ± 0.8, **Figure 4C**), confirming abundant expression of functional NMDARs at feedback excitatory synapses on PV+ interneurons.

Our results so far argue that NMDARs mediate supralinear integration of uncaging-evoked responses in stratum oriens dendrites, and that synapses mediating feedback excitation of stratum oriens dendrites are enriched with NMDARs. Glutamate uncaging does not necessarily restrict NMDAR activation to synaptic receptors, leaving uncertain whether feedback innervation of PV+ interneurons is able to engage NMDARs under more physiological conditions. We therefore used the same optogenetic strategy, to ask whether feedback inputs from local CA1 pyramidal cells depolarize PV+ interneurons sufficiently to recruit NMDARs. We measured the contribution of NMDARs to optogenetically evoked EPSPs recorded in current clamp, whilst incrementing the light intensity through a duty cycle (**Figure 4D**). Perfusion of the NMDAR blocker D-AP5 significantly reduced both the average time-integral and the ratio of integral to peak of EPSPs evoked at the maximal light intensity ($P = 0.033$; $P = 0.014$; n=5), but not the peak EPSPs (**Figure 4E,F**). Furthermore, in line with cooperative postsynaptic voltage-dependent relief of $Mg^{2+}$ blockade, we observed a larger NMDAR contribution to EPSPs elicited by stronger light pulses (**Figure 4G**). Together, these experiments confirm that synaptic release at feedback inputs from CA1 pyramidal cells can elicit NMDAR-mediated depolarization of PV+ interneurons.

Excitatory neurons driven by a compact ‘hump’ of excitation in input space cooperated in recruiting NMDARs on the interneuron to a greater extent than equivalent excitation shuffled randomly in input space (**Figure 5D**). The disproportionate NMDAR activation by compact versus distributed excitation recapitulates multiple co-active synapses within a small region of the dendritic tree cooperating to relieve NMDARs from $Mg^{2+}$ blockade. Although individual pyramidal neurons fired sparsely, an effect of the gamma oscillation was to synchronize them so that the local depolarization was maximized.

Recruitment of NMDAR conductances in the interneuron also maintained sparse principal cell firing over several oscillatory cycles (Figure 5 – Figure Supplement 2). In contrast, without NMDARs, the hump of active principal cells broadened as the oscillation stabilized. Principal cells at the core of the hump of activity (as defined by synaptic location on the interneuron dendritic tree) thus preferentially influence the firing of the interneuron as a result of the recruitment of NMDARs. We propose, therefore, that NMDARs on PV+ interneurons contribute to maintaining a sharp assembly representation, dependent on the spatial arrangement of active synapses on the dendritic tree of the interneuron.

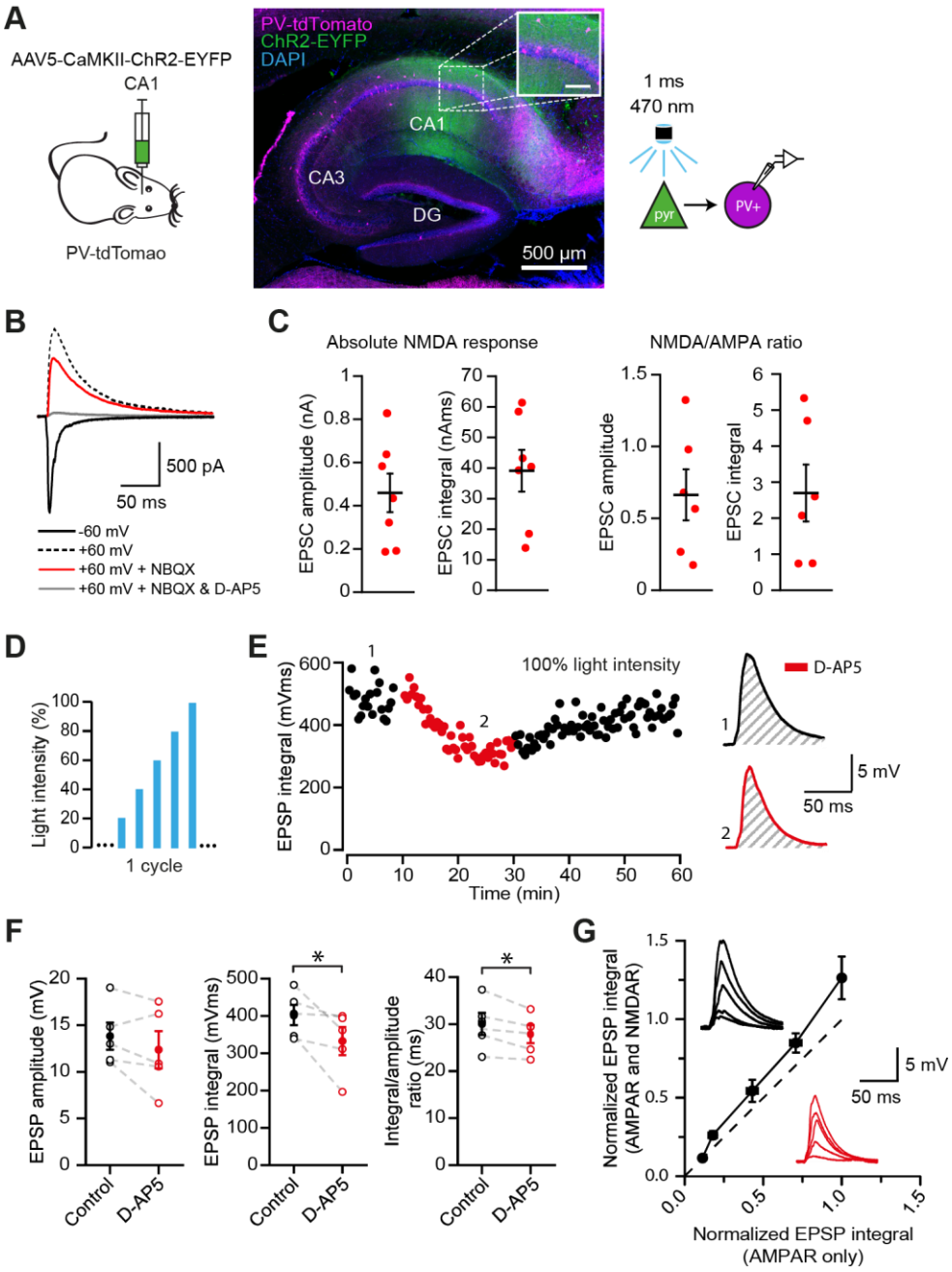


**Figure 4. NMDAR recruitment at CA1 pyramidal cell feedback connections onto PV+ interneurons.**

(**A**) Schematic of viral injections into dorsal CA1 of PV-tdTomato mice (left), and confocal image of a sagittal hippocampal slice showing selective ChR2-EYFP expression in CA1 pyramidal cells (middle, inset scale: 100 µm). Right: schematic of optogenetic patch clamp experiments. (**B**) Example traces of light-evoked feedback EPSCs in a PV+ interneuron held at -60 mV (black), +60 mV (black dashed), +60mV with application of NBQX (red) or +60mV with NBQX and D-AP5 in voltage clamp. (**C**) Quantification of absolute NMDAR-mediated feedback EPSCs (amplitude and integral, left, n = 7) and NMDAR/AMPAR ratios

(amplitude and integral, right, n = 6), measured from voltage clamp experiments as in (B). Black bars indicate mean ± SEM.
(**D**) Schematic of optogenetic stimulation protocol for current clamp experiments: light power was cycled from 20% to 100% of power for maximal response (see methods).
(**E**) EPSP integral of maximal response over time, with 20 min application of D-AP5 (red).
(**F**) EPSP amplitude, EPSP integral and integral/amplitude ratio in the presence (red) or absence (black) of D-AP5 (n = 5, one-tailed *t*-tests; control = average of baseline and wash). Filled circles and error bars indicate mean ± SEM.
(**G**) Normalized EPSP integrals (black example traces) vs normalized EPSP integrals in the presence of D-AP5 (red example traces), for all stimulation intensities (n = 5).

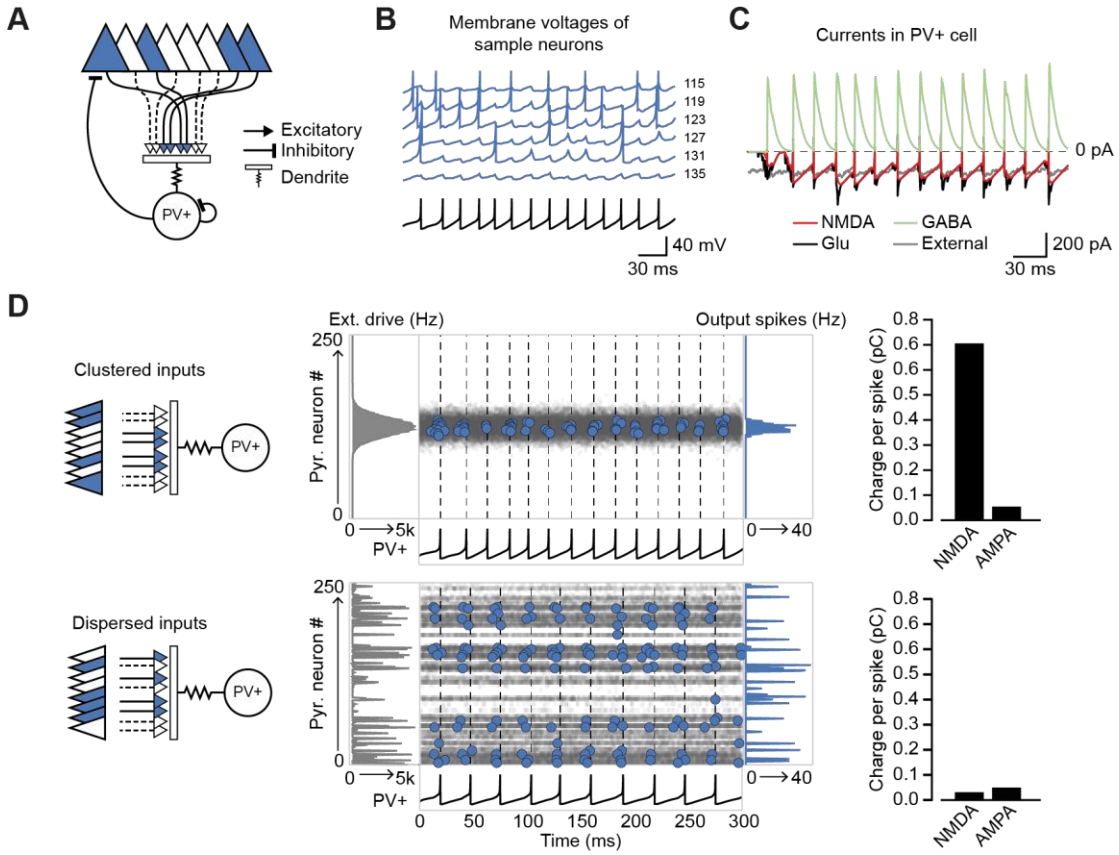


**Figure 5. Network architecture and NMDAR recruitment at feedback connections.**
(**A**) Schematic of network structure.
(**B**) Voltage traces of interneuron (black) and principal cells (blue, cell # at right) during network simulation. The network was driven by an asynchronous barrage of spikes, maximal in cell #125 (‘clustered’ input).

(**C**) Corresponding currents in interneuron. Red: NMDAR currents from principal cells; green: GABAR currents from autaptic PV+ cell connections; black: sum of NMDAR and AMPAR currents from principal cells; gray: AMPAR currents from external drive.
(**D**) Left: schematic showing cell assemblies receiving clustered (top) or dispersed (bottom) external inputs, and middle: corresponding summary plots of network simulation showing external drive input distribution (gray), pyramidal cell firing (blue, circles), and interneuron firing (black, and vertical dashed lines). Right: average NMDAR and AMPAR charge in interneuron per principal neuron spike. (Autaptic and feedback connections from PV+ cells are omitted from the schematic for clarity.)

Next, we simulated two similar networks mutually inhibiting one another (Geisler et al., 2007; Trouche et al., 2016) to understand how NMDARs in the inhibitory neurons could affect competition among cell assemblies. When one network received a stable and compact hump of excitation (again, with input space defined by location on the interneuron dendritic tree) it was much more likely to 'win' than a competing network receiving an equal amount of excitation that was dispersed (**Figure 6A**). This effect results from the additional interneuron depolarization mediated by NMDARs which were recruited by clustered synapses. The tendency for the network receiving a hump of excitation to win disappeared when NMDARs were removed from the inhibitory neurons (**Figure 6B,C**).

Finally, we explored the ability of the combined network to 'lock' onto one of two inputs of similar strength and compactness presented to the two sub-networks (**Figure 7**). An ethologically relevant analogous task in humans is the ability to stabilize perception of a Necker cube (**Figure 7A**). Although we make no claim as to how this task is solved, it exemplifies a situation where two sensory or cognitive representations compete for recruitment of a network. The net excitatory external drive to each of the sub-networks was allowed to fluctuate independently with time **(Figure 7B)**. As a result of this stochastic variability in the external drive strength, and neuronal accommodation, the combined network intermittently 'flipped' between the two inputs. However, the frequency of flipping increased steeply when the normalized conductance of NMDARs was decreased in the inhibitory neurons, resulting in a flickering of the dominant assemblies (**Figure 7C**). In contrast, the frequency of flipping was relatively unaffected by reducing the AMPAR conductance (**Figure 7D**). Because gamma oscillations in the hippocampus are nested within slower theta oscillations (Chrobak and Buzsáki, 1998), we repeated the simulations while modulating the external drive with a theta oscillation. This yielded qualitatively similar results (Figure 7 – Figure Supplement 1). We thus conclude that NMDAR-mediated cooperative interactions among clustered synapses on an interneuron stabilize cell assemblies.

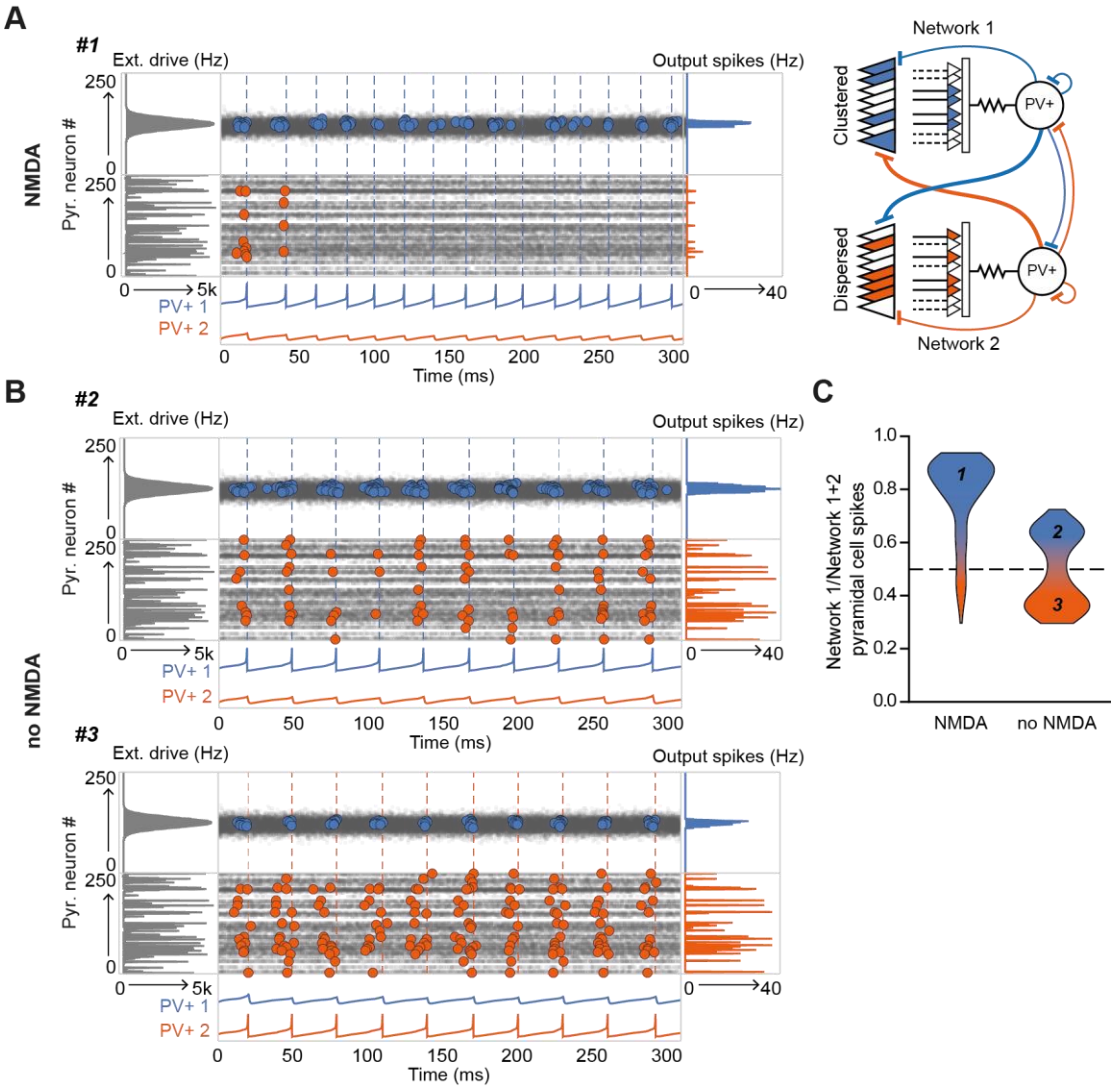


**Figure 6. The role of NMDARs at feedback connections in cell assembly competition.**

(**A**) Right: schematic showing competing cell assemblies with clustered (blue) or dispersed (orange) inputs; left: example simulation of lateral inhibition between these subnetworks with NMDARs at feedback connections to interneuron (input distribution: gray; pyramidal cell firing: blue/orange, circles; interneuron firing: blue/orange spikes and vertical dashed lines). The network receiving the clustered input out-competed the network receiving the dispersed input.

(**B**) Same as (A) but without NMDARs at feedback connections, showing, in one case the network receiving clustered input firing more than the network receiving dispersed input (top), and in the other case the network receiving dispersed input winning (bottom).

(**C**) Summary of 250 simulations showing ratio of principal cell spikes for each subnetwork with and without NMDARs at feedback inputs onto interneuron. Numbers correspond to simulations illustrated in (A) and (B).

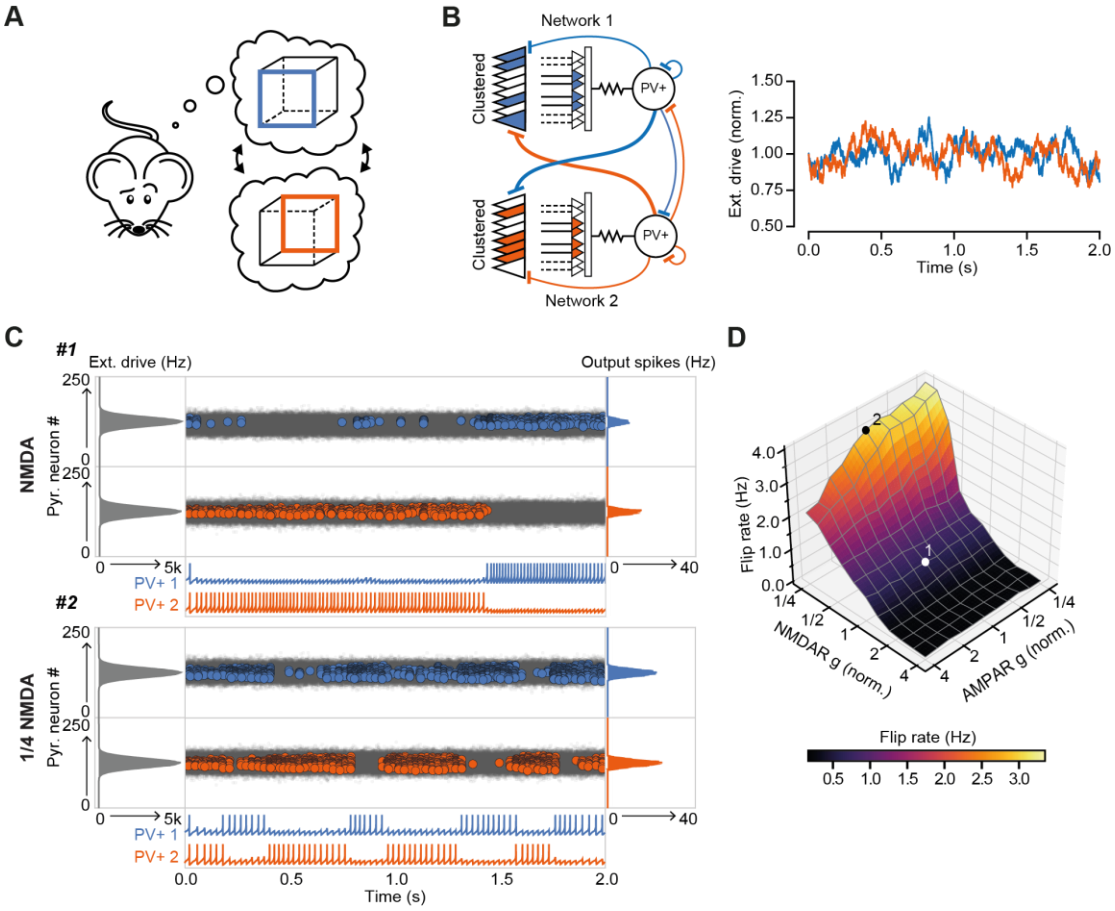


**Figure 7. The role of NMDARs at feedback connections in cell assembly stability.**

(**A**) Cartoon illustrating a bistable neural representation.

(**B**) Schematic of competing subnetworks both receiving clustered inputs (left) with random fluctuations in external input strength (plotted right).

(**C**) Example simulation of network activity with NMDARs at synapses on interneurons (top), and with NMDARs scaled down to 25% of baseline (bottom). Input distribution: gray; pyramidal cell firing: blue/orange, circles; interneuron firing: blue/orange spikes. Although the dominant networks flipped spontaneously in both cases, the frequency of flipping was much higher with the down-scaled NMDARs.

(**D**) Plot of network flip rate vs NMDAR and AMPAR conductance. White point (1): baseline NMDAR simulation parameters; black point (2): NMDARs down-scaled to 25%.

## Discussion

The present study shows that clustered excitatory synapses on stratum oriens dendrites of CA1 PV+ interneurons interact supralinearly, challenging the view that they act as linear integrators of synaptic inputs (see also (Tzilivaki et al., 2019)). The high impedance of stratum oriens dendrites, which are innervated by axon collaterals of local pyramidal neurons, facilitates the cooperative recruitment of NMDARs. In addition, voltage clamp experiments show a larger NMDAR/AMPAR ratio at feedback inputs than at feed-forward inputs. We place these results in the context of cell assembly competition by including nonlinear feedback integration in a spiking neural network model. NMDARs at synapses on a simulated feedback interneuron allow multiple principal cells co-innervating a subset of its input space, reminiscent of a dendritic branch, to interact cooperatively in recruiting the interneuron. We show that cooperative assemblies are more able to efficiently engage interneurons in the inhibition of rival competing assembly representations. Furthermore, we report that inclusion of NMDAR conductances at feedback synapses stabilizes cell assemblies, allowing the network to 'lock' on to an input. An adaptive role of NMDARs in feedback excitation of PV+ interneurons can therefore be to facilitate the emergence of strong and stable cell assemblies.

Extrapolating from the behavior of a spiking neural network model to information processing clearly depends on a number of assumptions, not least that the principles underlying NMDAR-dependent input integration observed in CA1 PV+ interneurons apply generally throughout the brain, and that clustering of homotopic inputs on inhibitory dendritic segments obeys the same rules as in excitatory neurons (Iacaruso et al., 2017; Wilson et al., 2016). In addition, while PV+ cells predominantly show NMDAR-independent anti-Hebbian LTP (Lamsa et al., 2007), dependent on calcium-permeable AMPARs, feedback synapses also display NMDAR-dependent Hebbian plasticity rules (Le Roux et al., 2013). In this study we isolate the integrative properties of NMDARs from their role in synaptic plasticity, but it is expected that plasticity mechanisms may also contribute to the network phenomena described here. For example, NMDAR-dependent plasticity, which could be induced by cooperative feedback synaptic integration, would allow PV+ interneurons to be wired into stimulus-specific ensembles (Khan et al., 2018). Overall, therefore, NMDAR-dependent supralinear integration in the feedback inhibitory loop potentially expands the computational power of a canonical cortical motif.

Selective knockdown of NMDARs in PV+ interneurons has previously been shown to cause a range of functional impairments, including working-memory deficits and a reduction in the precision of hippocampal spatial representations (Korotkova et al., 2010). The network simulations presented here provide a mechanistic explanation for some of these results, in particular, a reduction in spatial information conveyed by principal cell spiking (Korotkova et al., 2010). Other studies highlight a role for PV+ cells and inhibition in cell-assembly competition: in the visual cortex PV+ inhibition

increases assembly similarity (Agetsuma et al., 2018) and in the hippocampus silencing of a dominant assembly was shown to uncover an alternative previously inhibited assembly (Trouche et al., 2016). The present study indicates that NMDARs may be integral to these functions.

Our network simulation results also resonate with multiple convergent findings that implicate PV+ cell NMDAR hypofunction at the centre of schizophrenia pathophysiology (Bygrave et al., 2016; Lisman et al., 2008; Nakazawa et al., 2012). For instance, NMDAR blockers have been shown to recapitulate some features of schizophrenia in healthy individuals (Krystal et al., 1994). When coupled with the observation that NMDAR antagonists cause a net disinhibition of principal cell activity (Homayoun and Moghaddam, 2007; Jackson et al., 2004), it has been suggested that cortical circuits are especially vulnerable to failure of NMDAR-mediated signalling in PV+ interneurons. Moreover, post-mortem studies have revealed a selective loss of PV+ interneurons in people with schizophrenia (Lewis et al., 2012) and overexpression of Neuregulin 1, a leading schizophrenia susceptibility gene, is associated with a reduction of NMDARs on PV+ cells (Kotzadimitriou et al., 2018). Destabilisation of dominant neuronal assemblies, as shown here to result from impaired NMDAR signalling on PV+ interneurons, may thus explain a failure of sensory gating (Javitt and Freedman, 2015) and evidence for reduced cognitive control, for instance in the Necker cube test (McBain et al., 2011), in schizophrenia.

Feedback inhibition, such as that mediated by PV+ interneurons, is thought to be critical for preventing runaway excitation. Indeed, a failure of feedback inhibitory restraint is a major factor in the emergence of pathological states such as epileptic seizures. Given the importance of inhibition, how then do PV+ interneurons participate in assemblies that are composed of cells that they also regulate? One possibility is that PV+ cells are ‘transient allies’ (Buzsáki, 2010), only aligning with principal cell assemblies over short time windows and at specific times. For example, in a recent study of circuit changes in the visual cortex during learning, PV+ cells were found to become more selective to task-relevant stimuli by increasing their coupling to stimuli selective principal cells and becoming less influenced by the general activity of the remaining surrounding network (Khan et al., 2018).

It is worth noting that feedback interneurons operating over longer time scales, for example somatostatin-positive oriens-lacunosum/moleculare interneurons, or cholecystokinin-expressing basket cells, may also be suited to mediate assembly competition. However, once recruited they would disengage more slowly because they integrate principal cell firing over a longer time frame. In contrast, PV+ cell firing is thought to define the period for gamma oscillations. As a result, NMDARs on PV+ interneurons are ideally suited to allow for stable assemblies while the stimulus is constant, but also allow for quick switching if the nature of the stimulus changes.

Recurrent connections between PV+ interneurons and local pyramidal cell circuits are found throughout the brain. A challenge for future studies will be to establish whether feedback connections outside of hippocampal area CA1 also display NMDAR-dependent supralinear feedback integration. Furthermore, experiments acutely and specifically blocking NMDARs at feedback synapses onto PV+ cells, as opposed to nonspecific knockdown of all PV+ cell NMDARs during development, will be necessary in order to fully characterize the importance of PV+ cell NMDAR processing *in vivo*. Taken together, our results expand the computational role of NMDARs on PV+ cells, providing a parsimonious mechanism uniting a number of hitherto unexplained observations, relating to both basic neuronal network function and pathophysiology.

**Acknowledgements**
We are grateful to members of the Experimental Epilepsy Group at the UCL Institute of Neurology, in particular Kaiyu Zheng, and also to Peter Latham and Arnd Roth for advice and technical assistance. This work was supported by the Wellcome Trust, the Medical Research Council and the Brain Research Trust.

**Competing interests**
The authors declare no competing interests.

**References**

Agetsuma M, Hamm JP, Tao K, Fujisawa S, Yuste R. 2018. Parvalbumin-Positive Interneurons Regulate Neuronal Ensembles in Visual Cortex. *Cereb Cortex N Y N 1991* **28**:1831–1845. doi:10.1093/cercor/bhx169

Amaral DG, Dolorfo C, Alvarez-Royo P. 1991. Organization of CA1 projections to the subiculum: a PHA-L analysis in the rat. *Hippocampus* **1**:415–435. doi:10.1002/hipo.450010410

Bartos M, Vida I, Frotscher M, Meyer A, Monyer H, Geiger JRP, Jonas P. 2002. Fast synaptic inhibition promotes synchronized gamma oscillations in hippocampal interneuron networks. *Proc Natl Acad Sci U S A* **99**:13222–7. doi:10.1073/pnas.192233099

Bezaire MJ, Soltesz I. 2013. Quantitative assessment of CA1 local circuits: knowledge base for interneuron-pyramidal cell connectivity. *Hippocampus* **23**:751–785. doi:10.1002/hipo.22141

Bowie D, Lange GD, Mayer ML. 1998. Activity-dependent modulation of glutamate receptors by polyamines. *J Neurosci*.

Branco T, Clark BA, Häusser M. 2010. Dendritic discrimination of temporal input sequences in cortical neurons. *Science* **329**:1671–1675.

Buzsáki G. 2010. Neural Syntax: Cell Assemblies, Synapsembles, and Readers. *Neuron* **68**:362–385. doi:10.1016/j.neuron.2010.09.023

Bygrave AM, Masiulis S, Nicholson E, Berkemann M, Barkus C, Sprengel R, Harrison PJ, Kullmann DM, Bannerman DM, Kätzel D. 2016. Knockout of

NMDA-receptors from parvalbumin interneurons sensitizes to schizophrenia-related deficits induced by MK-801. *Transl Psychiatry* **6**:e778. doi:10.1038/tp.2016.44

Carlén M, Meletis K, Siegle JH, Cardin JA, Futai K, Vierling-Claassen D, Rühlmann C, Jones SR, Deisseroth K, Sheng M, Moore CI, Tsai L-H. 2012. A critical role for NMDA receptors in parvalbumin interneurons for gamma rhythm induction and behavior. *Mol Psychiatry* **17**:537–548. doi:10.1038/mp.2011.31

Carnevale NT, Hines ML. 2009. The NEURON Book. Cambridge University Press.

Chiovini B, Turi G, Katona G, Kaszás A, Pálfi D, Maák P, Szalay G, Szabó M, Szabó G, Szadai Z, Káli S, Rózsa B. 2014. Dendritic Spikes Induce Ripples in Parvalbumin Interneurons during Hippocampal Sharp Waves. *Neuron* **82**:908–924. doi:10.1016/j.neuron.2014.04.004

Chrobak JJ, Buzsáki G. 1998. Gamma oscillations in the entorhinal cortex of the freely behaving rat. *J Neurosci Off J Soc Neurosci* **18**:388–398.

Coyle JT. 2012. NMDA receptor and schizophrenia: A brief history. *Schizophr Bull* **38**:920–926. doi:10.1093/schbul/sbs076

Cuntz H, Forstner F, Borst A, Häusser M. 2010a. One rule to grow them all: a general theory of neuronal branching and its practical application. *PLoS Comput Biol* **6**. doi:10.1371/journal.pcbi.1000877

Cuntz H, Forstner F, Borst A, Häusser M. 2010b. One rule to grow them all: a general theory of neuronal branching and its practical application. *PLoS Comput Biol* **6**.

de Almeida L, Idiart M, Lisman JE. 2009. A second function of gamma frequency oscillations: an E%-max winner-take-all mechanism selects which cells fire. *J Neurosci Off J Soc Neurosci* **29**:7497–7503. doi:10.1523/JNEUROSCI.6044-08.2009

delPino I, García-Frigola C, Dehorter N, Brotons-Mas JR, Alvarez-Salvado E, MartínezdeLagrán M, Ciceri G, Gabaldón MV, Moratal D, Dierssen M, Canals S, Marín O, Rico B. 2013. Erbb4 Deletion from Fast-Spiking Interneurons Causes Schizophrenia-like Phenotypes. *Neuron* **79**:1152–1168. doi:10.1016/j.neuron.2013.07.010

Deuchars J, Thomson AM. 1996. CA1 pyramid-pyramid connections in rat hippocampus in vitro: Dual intracellular recordings with biocytin filling. *Neuroscience* **74**:1009–1018. doi:10.1016/S0306-4522(96)00251-5

Ferguson KA, Huh CYL, Amilhon B, Williams S, Skinner FK. 2014. Simple, biologically-constrained CA1 pyramidal cell models using an intact, whole hippocampus context. *F1000Research* **3**:104. doi:10.12688/f1000research.3894.1

Ferguson KA, Huh CYL, Amilhon B, Williams S, Skinner FK. 2013. Experimentally constrained CA1 fast-firing parvalbumin-positive interneuron network models exhibit sharp transitions into coherent high frequency rhythms. *Front Comput Neurosci* **7**:144. doi:10.3389/fncom.2013.00144

Gasparini S. 2006. State-Dependent Dendritic Computation in Hippocampal CA1 Pyramidal Neurons. *J Neurosci* **26**:2088–2100. doi:10.1523/JNEUROSCI.4428-05.2006

Geiger JR, Lübke J, Roth A, Frotscher M, Jonas P. 1997. Submillisecond AMPA receptor-mediated signaling at a principal neuron-interneuron synapse. *Neuron* **18**:1009–1023.

Geisler C, Robbe D, Zugaro M, Sirota A, Buzsáki G. 2007. Hippocampal place cell assemblies are speed-controlled oscillators. *Proc Natl Acad Sci* **104**:8149–8154.

Gulyás AI, Megías M, Emri Z, Freund TF. 1999. Total number and ratio of excitatory and inhibitory synapses converging onto single interneurons of different types in the CA1 area of the rat hippocampus. *J Neurosci Off J Soc Neurosci* **19**:10082–10097.

Hines ML, Carnevale NT. 1997. The NEURON simulation environment. *Neural Comput* **9**:1179–1209. doi:10.1162/neco.1997.9.6.1179

Homayoun H, Moghaddam B. 2007. NMDA receptor hypofunction produces opposite effects on prefrontal cortex interneurons and pyramidal neurons. *J Neurosci Off J Soc Neurosci* **27**:11496–11500. doi:10.1523/JNEUROSCI.2213-07.2007

Hu H, Jonas P. 2014. A supercritical density of Na(+) channels ensures fast signaling in GABAergic interneuron axons. *Nat Neurosci* **17**:686–693.

Hu H, Martina M, Jonas P. 2010. Dendritic mechanisms underlying rapid synaptic activation of fast-spiking hippocampal interneurons. *Science* **327**:52–58. doi:10.1126/science.1177876

Iacaruso MF, Gasler IT, Hofer SB. 2017. Synaptic organization of visual space in primary visual cortex. *Nature* **547**:449–452. doi:10.1038/nature23019

Izhikevich EM. 2003. Simple model of spiking neurons. *IEEE Trans Neural Netw* **14**:1569–1572. doi:10.1109/TNN.2003.820440

Jackson ME, Homayoun H, Moghaddam B. 2004. NMDA receptor hypofunction produces concomitant firing rate potentiation and burst activity reduction in the prefrontal cortex. *Proc Natl Acad Sci U S A* **101**:8467–8472. doi:10.1073/pnas.0308455101

Javitt DC, Freedman R. 2015. Sensory processing dysfunction in the personal experience and neuronal machinery of schizophrenia. *Am J Psychiatry* **172**:17–31. doi:10.1176/appi.ajp.2014.13121691

Jonas P, Bischofberger J, Fricker D, Miles R. 2004. Interneuron Diversity series: Fast in, fast out – temporal and spatial signal processing in hippocampal interneurons. *Trends Neurosci* **27**:30–40.

Kerlin AM, Andermann ML, Berezovskii VK, Reid RC. 2010. Broadly tuned response properties of diverse inhibitory neuron subtypes in mouse visual cortex. *Neuron* **67**:858–871. doi:10.1016/j.neuron.2010.08.002

Khan AG, Poort J, Chadwick A, Blot A, Sahani M, Mrsic-flogel TD, Hofer SB. 2018. selectivity and interactions of GABAergic interneuron classes in visual cortex. *Nat Neurosci* **21**. doi:10.1038/s41593-018-0143-z

Korotkova T, Fuchs EC, Ponomarenko A, von Engelhardt J, Monyer H. 2010. NMDA receptor ablation on parvalbumin-positive interneurons impairs hippocampal synchrony, spatial representations, and working memory. *Neuron* **68**:557–569. doi:10.1016/j.neuron.2010.09.017

Kotzadimitriou D, Nissen W, Paizs M, Newton K, Harrison PJ, Paulsen O, Lamsa K. 2018. Neuregulin 1 Type-I over-Expression Is Associated with Reduced NMDA Receptor-Mediated Synaptic Signaling in Hippocampal Interneurons Expressing PV or CCK. *eNeuro* **5**. doi:10.1523/ENEURO.0418-17.2018

Krystal J, Karper L, Seibyl J, Freeman G, Delaney R, Bremner D, Heninger G, Bowers M, Charney D. 1994. Subanesthetic effects of the NMDA antagonist, ketamine, in humans: psychotomimetic, perceptual, cognitive, and neuroendocrine effects. *Arch Gen Psychiatry* **51**:199–214. doi:10.1017/CBO9781107415324.004

Lamsa KP, Heeroma JH, Somogyi P, Rusakov DA, Kullmann DM. 2007. Anti-hebbian long-term potentiation in the hippocampal feedback inhibitory circuit. *Science* **315**:1262–1266. doi:10.1126/science.1137450

Le Roux N, Cabezas C, Böhm UL, Poncer JC. 2013. Input-specific learning rules at excitatory synapses onto hippocampal parvalbumin-expressing interneurons. *J Physiol* **591**:1809–22. doi:10.1113/jphysiol.2012.245852

Lewis DA, Curley AA, Glausier JR, Volk DW. 2012. Cortical parvalbumin interneurons and cognitive dysfunction in schizophrenia. *Trends Neurosci* **35**:57–67. doi:10.1016/j.tins.2011.10.004

Lisman JE, Coyle JT, Green RW, Javitt DC, Benes FM, Heckers S, Grace AA. 2008. Circuit-based framework for understanding neurotransmitter and risk gene interactions in schizophrenia. *Trends Neurosci* **31**:234–242. doi:10.1016/j.tins.2008.02.005

Losonczy A, Magee JC. 2006. Integrative properties of radial oblique dendrites in hippocampal CA1 pyramidal neurons. *Neuron* **50**:291–307. doi:10.1016/j.neuron.2006.03.016

Matta JA, Pelkey KA, Craig MT, Chittajallu R, Jeffries BW, McBain CJ. 2013. Developmental origin dictates interneuron AMPA and NMDA receptor subunit composition and plasticity. *Nat Neurosci* **16**:1032–1041. doi:10.1038/nn.3459

McBain R, Norton DJ, Kim J, Chen Y. 2011. Reduced cognitive control of a visually bistable image in schizophrenia. *J Int Neuropsychol Soc* **17**:551–556. doi:10.1017/S1355617711000245

Mel BW. 1992. NMDA-Based Pattern Discrimination in a Modeled Cortical Neuron. *Neural Comput* **4**:502–517. doi:10.1162/neco.1992.4.4.502

Nakazawa K, Zsiros V, Jiang Z, Nakao K, Kolata S, Zhang S, Belforte JE. 2012. GABAergic interneuron origin of schizophrenia pathophysiology. *Neuropharmacology* **62**:1574–1583. doi:10.1016/j.neuropharm.2011.01.022

Nörenberg A, Hu H, Vida I, Bartos M, Jonas P. 2010. Distinct nonuniform cable properties optimize rapid and efficient activation of fast-spiking GABAergic

interneurons. *Proc Natl Acad Sci U S A* **107**:894–899. doi:10.1073/pnas.0910716107

Poirazi P, Mel BW. 2001. Impact of active dendrites and structural plasticity on the memory capacity of neural tissue. *Neuron* **29**:779–796. doi:10.1016/S0896-6273(01)00252-5

Pouille F, Marin-Burgin A, Adesnik H, Atallah B V, Scanziani M. 2009. Input normalization by global feedforward inhibition expands cortical dynamic range. *Nat Neurosci* **12**:1577–1585. doi:10.1038/nn.2441

Pouille F, Scanziani M. 2004. Routing of spike series by dynamic circuits in the hippocampus. *Nature* **429**:717–723. doi:10.1038/nature02615

Pouille F, Scanziani M. 2001. Enforcement of temporal fidelity in pyramidal cells by somatic feed-forward inhibition. *Science* **293**:1159–63. doi:10.1126/science.1060342

Roth A, van Rossum MCW. 2009. Modeling Synapses. *Comput Model Methods Neurosci* **06**:139–160. doi:10.7551/mitpress/9780262013277.003.0007

Stuart GJ, Spruston N. 2015. Dendritic integration: 60 years of progress. *Nat Neurosci* **18**:1713–1721. doi:10.1038/nn.4157

Trouche S, Perestenko P V, van de Ven GM, Bratley CT, McNamara CG, Campo-Urriza N, Black SL, Reijmers LG, Dupret D. 2016. Recoding a cocaine-place memory engram to a neutral engram in the hippocampus. *Nat Neurosci* **19**:564–567. doi:10.1038/nn.4250

Tzilivaki A, Kastellakis G, Poirazi P. 2019. Challenging the point neuron dogma: FS basket cells as 2-stage nonlinear integrators. *Nat Commun* **10**:3664. doi:10.1038/s41467-019-11537-7

Wang XJ, Buzsáki G. 1996. Gamma oscillation by synaptic inhibition in a hippocampal interneuronal network model. *J Neurosci* **16**:6402–6413.

Williams SR, Mitchell SJ. 2008. Direct measurement of somatic voltage clamp errors in central neurons. *Nat Neurosci* **11**:790–798.

Wilson DE, Whitney DE, Scholl B, Fitzpatrick D. 2016. Orientation selectivity and the functional clustering of synaptic inputs in primary visual cortex. *Nat Neurosci* **19**:1003–1009. doi:10.1038/nn.4323

**Materials and Methods**

Animals

Hippocampal slices were obtained from postnatal day 14 – 24 male and female mice, or from 2-3 month old male and female mice (optogenetic experiments), expressing tdTomato in PV+ interneurons. Experimental mice were obtained by crossing homozygous mice expressing Cre under the PV promoter (Jackson Labs: B6;129P2-Pvalb$^{tm1(cre)Arbr}$) with homozygous Ai9 Cre reporter mice (Jackson Labs: B6.Cg-*Gt(ROSA)26Sor*$^{tm9(CAG\text{-}tdTomato)Hze}$). Animals were group-housed under a non-reversed 12 h light/dark cycle, and allowed access to food and water *ad libitum*. All procedures were carried out in accordance with the UK Animals (Scientific Procedures) Act, 1986.

Surgery for viral injections

Mice (minimum age: 6 weeks) were anaesthetized with isoflurane and virus (AAV5-CaMKIIa-hChR2(H134R)-EYFP) was stereotaxically injected into the dorsal CA1 region of both hippocampi using a Hamilton syringe. The injection coordinates were 2.15 mm caudal and 1.4 mm lateral of Bregma, and 1.2 and 1.0 mm deep from the pia. 50 nl of virus was injected at each site at a rate of 100 nl/min, and the needle was left in place for 5 minutes following injections before withdrawal. Slices were prepared for experiments after a minimum of three weeks post-surgery.

Slice preparation and electrophysiology

Acute sagittal brain slices (300 μm) were prepared using a Vibratome (Leica VT1200 S). Slices were cut in an ice-cold artificial cerebrospinal fluid (ACSF) solution, containing (in mM): NaCl (119), KCl (2.5), $NaH_2PO_4$ (1.25), $NaHCO_3$ (25), glucose (20), $CaCl_2$ (1.5), $MgSO_4$ (1.3), and saturated with 95% $O_2$, 5% $CO_2$. Slices were allowed to recover at 32˚C for 15 min after slicing, before subsequent storage in ACSF at room temperature. Older mice (>1 month) were transcardially perfused with ice-cold sucrose-based ACSF solution, containing (in mM): sucrose (75), NaCl (87), KCl (2.5), $NaH_2PO_4$ (1.25), $NaHCO_3$ (25), glucose (25), $CaCl_2$ (0.5), $MgCl_2$ (7), and saturated with 95% $O_2$, 5% $CO_2$. Slices were cut in the same solution, and left to recover at 32˚C for 15 min, before being transferred to normal ACSF (same as above but with 2.5 mM $CaCl_2$) for storage at room temperature. All experiments were carried out in ACSF maintained at 30˚ – 32˚C and perfused at 2–3 ml/min. Recordings were made from dorsal hippocampal slices. For dissection of AMPAR and NMDAR components at feedforward and feedback synapses (**Figure 3A,B**) a modified ACSF containing 0.1 mM $MgSO_4$ was used to partially relieve $Mg^{2+}$ blockade of NMDARs at rest. NMDARs and AMPARs were sequentially blocked with D-AP5 (100 μM) and 2,3-dihydroxy-6-nitro-7-sulfamoyl-benzo[f]quinoxaline-2,3-dione (NBQX, 10 μM), respectively. Picrotoxin (100 μM) and CGP 55845 (1 μM) were included throughout these experiments, as well as the HCN channel blocker ZD

7288 (30 μM), which was included in order to hyperpolarize pyramidal cells and decrease network excitability. Picrotoxin (100 μM) and CGP 55845 (1 μM) were also included throughout the optogenetic experiments (**Figure 4**). For blockade of NMDARs or $Na^+$ channels during uncaging experiments (**Figure 2**) D-AP5 (100 μM) or TTX (0.1 μM) were used, respectively.

Fluorescence-guided somatic whole-cell recordings were obtained from PV+ interneurons and pyramidal cells using a Multiclamp 700B amplifier (Molecular Devices), filtered at 5 kHz, and digitized at 20 kHz (National Instruments PCI-6221), with custom software written in LabVIEW. Patch pipettes of 3 – 4 MΩ resistance were filled with KGluconate- or CsGluconate-based internal solution for current clamp or voltage clamp experiments, respectively. These solutions contained (in mM): KGluconate (140), KOH-HEPES (10), EGTA (0.2), NaCl (8), Mg-ATP (2), Na-GTP (0.3) or CsGluconate (125), HCsO-HEPES (10), EGTA (0.2), NaCl (8), Mg-ATP (4), Na-GTP (0.33), Na-Phosphocreatine (10), TEA-Cl (5) QX314 (5). Cells were held at -60 mV or +60 mV during voltage-clamp experiments (**Figure 3A,B**, and **Figure 4B,C**). All other experiments were performed in current-clamp mode, and current was continuously injected to maintain cell membrane between -65 and -70 mV. The series resistance during voltage clamp recordings was <15 MΩ and during current clamp recordings was < 25 MΩ. For field stimulation experiments, concentric bipolar stimulating electrodes (FHC) coupled to constant current stimulators (Digitimer) were placed in the alveus and stratum radiatum in order to evoke responses from feedback and feedforward inputs, respectively (Pouille and Scanziani, 2004). Stimuli were delivered to each pathway at 0.05 Hz, and alternated between the pathways. Optogenetic responses were elicited using 470 nm light pulses (1 ms, 1-15 mW) at 0.2 Hz, generated by an LED light-source (ThorLabs) and delivered through a 40X objective lens (Olympus). The light power necessary to elicit maximal and minimal responses was identified for each cell, and the difference in power was divided by 5 to define the 5 stimulation strengths (20%, 40%, 60%, 80% and 100%) used in each cycle. Maximal responses were identified as the maximum response elicited without generating an action potential (typically ≤ 15 mV), and minimal responses were the smallest response visible.

Two-photon imaging and uncaging experiments

Slices were submerged in a perfusion chamber on an upright microscope (FV1000 BX61, Olympus). Simultaneous two-photon imaging and uncaging of MNI-caged glutamate was performed with two Ti-sapphire lasers tuned to 810 nm and 720 nm, for imaging and uncaging respectively (Mai-Tai, Spectra Physics; Chameleon, Coherent). MNI-caged-glutamate-TFA (3 mM; Femtonics) dissolved in the recording ACSF solution was perfused in a closed system.

Uncaging locations (range: 8 – 12, mean: 8.4 vs 8.5 sites in radiatum and oriens respectively) were selected either side of a dendritic region of interest, separated by 2

– 3 µm and within 1 µm of the dendrite. Uncaging-evoked EPSPs (uEPSPs) were evoked using 0.5 ms-long pulses of 720 nm laser-light. To account for differing depths of dendritic segments, uncaging-laser intensity was adjusted using a Pockels Cell (Conoptics). uEPSPs were first evoked by sequential stimulation of individual uncaging spots with an inter-stimulus interval of 200 ms. Uncaging locations (order chosen at random) were then stimulated at intervals of 1 ms, with 10 s delays between trials. Beginning with a single location, the number of uncaging locations was increased on successive trials until all locations were activated. The entire sequence was repeated between 2 and 5 times, without changing the order of uncaging locations, and the responses to each combination of uncaging locations were averaged. Arithmetic compound uEPSPs were constructed offline from the average of 5 – 8 responses to uncaging at each individual location, including a 1 ms waveform shift to match the experimental protocol, and compared to recorded uEPSPs. Uncaging times and locations were controlled by scanning software (Fluoview 1000V) and a pulse generator (Berkeley Nucleonics) coupled to the Pockels cell. Experiments were discontinued and excluded from analysis if photo-damage to PV+ cells was observed, or if physical drift occurred.

For experiments in which uncaging locations were placed across pairs of dendrites, uEPSPs were elicited from 12 locations in total, 6 on each dendrite. Glutamate was uncaged at locations across the two dendrites in 5 distinct patterns. Patterns 1 and 2 were on single dendrites (using alternate uncaging locations 1, 3, …,11 and 2, 4, …, 12), whereas patterns 3 – 5 ('mixed' dendrites) were across both dendrites (uncaging locations 1, 2, 3, 4, 5, 6; 4, 5, 6, 7, 8, 9; and 7, 8, 9, 10, 11, 12). For all patterns, locations on the same dendrite were activated with an interval of 2 ms, and waveforms were averaged across 4 repetitions. We constructed arithmetic compound uEPSPs for each pattern offline from the average of approximately 8 responses to uncaging at each individual location as above, and calculated the amplitude nonlinearity of the recorded vs arithmetic uEPSP. To compare between uESPSs evoked on single vs mixed dendrites we averaged the amplitude nonlinearity from patterns 1 – 2 and 3 – 5, respectively.

Quantification and statistical analysis

Data analysis was performed using custom code written in Python. The nonlinearity of responses recorded from uncaging at each dendritic location was quantified using the following equation:

$$\%\, nonlinearity = \sum_{i=2}^{n} \frac{\frac{Mi}{Ai} - 1}{n - 1} \cdot 100\% \qquad 1)$$

where $Mi$ is the amplitude of the $ith$ measured uEPSP (composed of $i$ individual uncaging spots), $Ai$ is the amplitude of the $ith$ constructed arithmetic summed uEPSP,

and $n$ is the total number of uncaging locations. For uEPSP integral analysis a Savitzky-Golay filter was applied to traces.

For analysis of NMDAR/AMPAR ratios in **Figure 3A**, the AMPAR-mediated response was calculated by subtracting the NMDAR-mediated response (recorded in NBQX) from the baseline EPSC. NMDAR and AMPAR charge were then calculated by integrating the first 500 ms or 20 ms, respectively, of these isolated traces. NMDAR/AMPAR ratios in **Figure 4C** were calculated as the ratio between the NMDAR-mediated response recorded at +60 mV in the presence of NBQX (with the +60 mV response in the presence of D-AP5 subtracted), and the AMPAR-mediated response recorded at -60 mV.

Statistical significance was assessed using Student's paired or unpaired *t*-tests. Data are presented as mean ± SEM, unless stated otherwise. Sample sizes were estimated to obtain 80% power to detect effects at $p<0.05$. *n* values are for cells.

Multi-compartmental modelling

Multi-compartmental modelling was performed with the NEURON 7.5 simulation environment (Hines and Carnevale, 1997). The soma and dendrites of a PV+ interneuron were reconstructed using the TREES toolbox in MATLAB (Cuntz et al., 2010a). The axon was not included in the reconstruction. As PV+ interneuron dendrites are generally smooth, addition of spines or correction of synaptic responses for spines was deemed unnecessary. The number of segments per section was constrained to odd numbers and set according to the d-lambda rule (Carnevale and Hines, 2009) to have a length no more than 10% of the alternating current length constant at 1 kHz. The model contained 500 segments in total with a maximal segment length of 8.7 μm.

The biophysical parameters were based on previously published models of dentate gyrus PV+ basket cells (Hu and Jonas, 2014; Nörenberg et al., 2010). The specific membrane capacitance ($C_m$) and intracellular resistance ($R_i$) were assumed to be spatially uniform (for values see Table 1). In contrast, the specific membrane resistance ($R_m$) was assumed to vary as a step function with distance from the soma. $R_m$ at distal dendrites was 10 times larger than at proximal dendrites, and $R_m$ was chosen so as to make the model cell's input resistance 78 MΩ, the mean experimentally recorded input resistance (78.6 ± 5.2 MΩ). The border between proximal and distal dendrites was defined to be 120 μm from the soma.

**Table 1: NEURON model parameters**

| Parameter | Proximal | Distal | Units |
|---|---|---|---|
| $C_m$ | 0.9 | 0.9 | $\mu$F cm$^{-2}$ |
| $R_{axial}$ | 170 | 170 | $\Omega$ cm |
| $R_m$ | 5.55 | 55.5 | k$\Omega$ |
| $e_{leak}$ | -65 | - | mV |
| $e_{gK}$ | -90 | - | mV |
| $e_{gNa}$ | 55 | - | mV |
| v shift | -12 | -12 | mV |
| $g_k$ dend | 300 | 300 | pS $\mu$m$^{-2}$ |
| $g_{Na}$ dend | 200 | 100 | pS $\mu$m$^{-2}$ |
| $g_{Na}$ soma | 2000 | - | pS $\mu$m$^{-2}$ |

Wang and Buzsaki (WB) $Na^+$ and $K^+$ channels were inserted in the model neuron to confer a fast-spiking action potential phenotype (Wang and Buzsáki, 1996). However, in order to produce a realistic firing frequency - current injection relationship a hyperpolarizing voltage shift was included in the WB implementation. The depolarized threshold of the WB mechanism has been discussed previously (Ferguson et al., 2013).

Subthreshold synaptic integration curves were produced by first finding all sites on the dendritic tree that were located between 40 and 190 µm from the soma. Simulations then closely followed the experimental protocol detailed above. At each dendritic site, 15 synapses were placed within a distance of 30 µm. Each synapse was activated individually and the arithmetic sum calculated from the somatic membrane potential. Synapses were then activated in increasing numbers, with an interval of 1 ms between activations, and the integral and amplitude of these measured responses compared to the calculated arithmetic responses. Quantification of dendritic nonlinearity was identical to that applied to experimental data.

Network modelling

**Single cell modelling**

For network simulations, PV+ interneurons and CA1 pyramidal cells were represented by two-dimensional Izhikevich model neurons (Izhikevich, 2003). Izhikevich models for these neurons have previously been parameterized from experimental data (Ferguson et al., 2014, 2013). In line with this previous work, the models were slightly modified to reproduce the narrow PV+ interneuron spike width, and had the following form:

$$C_m \frac{dv}{dt} = k(v - v_r)(v - v_t) - u + I_{applied}$$

$$\frac{du}{dt} = a[b(v - v_r) - u] \quad (2)$$

$$if\ v \geq v_{peak}\text{, set } v = c,\ u = u + d$$
$$\text{Where } k = k_{low} \text{ if } v \leq v_t; k = k_{high} \text{ if } v > v_t$$

The variable $v$ represents the membrane potential, and $u$ represents a slow 'refractory' current, that, aside from subthreshold effects governed by $b$, is increased by $d$ when the neuron fires, and decays at a rate determined by $a$. The parameter $C_m$ represents the membrane capacitance; $k$ is a scalar; $v_r$ is the resting membrane potential; $v_t$ is the instantaneous spiking threshold potential; $v_{peak}$ is the peak action potential voltage; $I_{applied}$ is the applied current, comprised of the sum of all synaptic inputs to the cell; $a$ is the recovery inverse time constant of the refractory current, u; $b$ is the sensitivity of $u$ to subthreshold voltage fluctuations; $c$ is the voltage reset value; and $d$ is the amount of current generated by the after-spike behavior. The values for all parameters of the network simulations are presented in Table 2.

**Synaptic modelling**

Synaptic connections between neurons were modelled as bi-exponential, conductance-based synapses (Roth and van Rossum, 2009), which can be written in the following differential form:

$$\begin{aligned} g^{chan}(v^{syn}) &= \frac{G^{chan}(v^{syn})}{\tau_1^{chan} - \tau_2^{chan}}(g_1^{chan} - g_2^{chan}) \\ \frac{dg_1^{chan}}{dt} &= \left(\delta^{chan}(t) - \frac{1}{\tau_1^{chan}} g_1^{chan}\right) \\ \frac{dg_2^{chan}}{dt} &= \left(\delta^{chan}(t) - \frac{1}{\tau_2^{chan}} g_2^{chan}\right) \\ G^{NMDA}(v^{syn}) &= \left(\frac{1}{2} tanh\left[\frac{v_i^{syn} + 50mV}{10mV}\right] + \frac{1}{2}\right) \\ G^{AMPA}(v^{syn}) &= G^{ext}(v^{syn}) = G^{GABA}(v^{syn}) = 1 \end{aligned} \tag{3}$$

Where $g^{chan}$ is the total synaptic conductance of a given channel family (composed of a rise term $g_1^{chan}$ and a decay term $g_2^{chan}$), $G^{chan}(v^{syn})$ is an eventual instantaneous voltage-gating term dependent on a local synaptic voltage $v^{syn}$(only relevant for NMDA channels; detailed in the next section), $\tau_1^{chan}$ is the rising exponential time constant, $\tau_2^{chan}$ is the decay exponential time constant, the variable $t$ is time. The function $\delta^{chan}(t)$ represents the input spike train. This is defined in continuous time in order to be agnostic to the numerical integration method used in the simulations. Specifically $\delta^{chan}(t)$ is modelled as:

$$\delta^{chan}(t) = \sum_{i}^{Nspikes} \delta(t - t_i) \tag{4}$$

Where $t_i$ are the times of the input spike arrivals for a particular receptor, and $\delta(t)$ is the continuous time Dirac delta distribution (0 everywhere apart from t=0 where it has infinite density and integrates to 1).

**NMDA receptor modelling**

NMDARs, present at the feedback connections from principal cells onto the interneuron, and the cooperative relief of NMDAR $Mg^{2+}$ block by co-active synaptic inputs, were modelled in an abstract manner. We assumed that all co-active inputs from the population of $n_{pyr}$ principal cells had a degree of cooperation, or functional clustering (Wilson et al., 2016), which was weighted by a distance matrix, $D^{n_{pyr} \times n_{pyr}}$. $D$ was defined as a Toeplitz matrix, with the *i*th element of the row vector $D_{\frac{n_{pyr}}{2}}$ equal to:

$$D_{\frac{n_{pyr}}{2},i} = \frac{1}{\sqrt{2\pi\ {\sigma_D}^2}} e^{-\frac{(i-n_{pyr}/2)^2}{2\ {\sigma_D}^2}} \tag{5}$$

Where ${\sigma_D}^2$ controlled the specificity of local cooperation. We then modelled the time evolution of the voltage of the local synaptic membrane patch, $v_i^{syn}$, with the following equation:

$$C_{syn}\frac{dv_i^{syn}}{dt} = k^{syn} I_i^{syn} + g^{leak}\left(e^{leak} - v_i^{syn}\right) \tag{6}$$

$$I_i^{syn} = \sum_{j=1}^{n_{pyr}} D_{i,j}\left(k_{pv+}^{AMPA} g_j^{AMPA} + k_{pv+}^{NMDA} g_j^{NMDA}(v_j^{syn})\right)\left(e^{glu} - v_i^{syn}\right)$$

Where $C_{syn}$ is the local patch membrane capacitance, $k^{syn}$ is a gain applied to the input current $I_i^{syn}$, $k_{pv+}^{chan}$ are gain constants defining each channel family synaptic strength onto the interneuron, $g^{leak}$ is a leak conductance with reversal potential $e^{leak}$.

Finally, the total current, $I_{applied}$, an interneuron receives is given by:

$$I_{applied} = \left(\sum_{i=1}^{n_{pyr}} k_{pv+}^{AMPA}\ g_i^{AMPA} + k_{pv+}^{NMDA} g_i^{NMDA}\left(v_i^{syn}\right) + k_{pv+}^{ext}\ g_i^{ext}\right)(e^{glu} - v) + \ k_{pv+}^{GABA}\left(\sum_{j=1}^{n_{pv+}} g_j^{GABA}\right)(e^{GABA} - v) \tag{7}$$

Accordingly, for the *i*th pyramidal cell the input current is more simply given by:

$$I_{Applied}^{i} = k_{pyr}^{ext}\ g_i^{ext}(e^{glu} - v) + \ k_{pyr}^{GABA}\left(\sum_{j=1}^{n_{pv+}} g_j^{GABA}\right)(e^{GABA} - v) \tag{8}$$

**External drive**

The external drive to the *i*th pyramidal neuron was modelled as a non-homogeneous Poisson process, in which the instantaneous rate of incoming spikes was given by an Ornstein–Uhlenbeck process with mean $\mu_{OU}$, volatility $\sigma_{OU}$ and time constant $\tau_{OU}$, multiplied by a Gaussian gain function representing the neuron position in the receptive field. The input of the PV+ interneurons was the scaled mean of all inputs to its afferent pyramidal cells. The peak mean $\mu_{OU}$ was 5000 spikes per second, $\tau_{OU}$ was 50 ms and $\sigma_{OU}$ was $\frac{1}{6}\mu_{OU}\sqrt{2\,\tau_{OU}}$ for the simulations in **Figure 7** and zero everywhere else (i.e. the Poisson rates were constant). These inputs are convolved with the AMPA synaptic conductance kernel defined in eq. (3) and parameterized by rise and decay time constants shown in table 2.

**Table 2: model neuron parameters for network modelling**

| Parameter | FS PV+ | Pyramidal | Units |
|---|---|---|---|
| $C_m$ | 90 | 115 | pF |
| $k_{low}$ | 1.7 | 0.1 | nS/mV |
| $k_{high}$ | 14 | 3.3 | nS/mV |
| $v_r$ | -60.6 | -65.8 | mV |
| $v_{peak}$ | 2.5 | 22.6 | mV |
| $v_t$ | -43.1 | -57 | mV |
| $a$ | 0.1 | 0.0012 | $ms^{-1}$ |
| $b$ | -0.1 | 3 | nS |
| $c$ | -67 | -65.8 | mV |
| $d$ | 0.1 | 10 | pA |
| $\tau_1^{AMPA}$ | 0.25 | 0.2 | ms |
| $\tau_2^{AMPA}$ | 0.77 | 1.7 | ms |
| $\tau_1^{GABA}$ | 0.27 | 0.3 | ms |
| $\tau_2^{GABA}$ | 1.7 | 3.5 | ms |
| $\tau_1^{NMDA}$ | 2 | - | ms |
| $\tau_2^{NMDA}$ | 60 | - | ms |
| $e^{glu}$ | 0 | 0 | mV |
| $e^{GABA}$ | -70 | -70 | mV |
| $\sigma_D{}^2$ | $0.015/(n_{pyr}{}^2)$ | - | - |
| $C_{syn}$ | 9 | - | pF |
| $k^{syn}$ | $3/n_{pyr}$ | - | - |
| $g^{leak}$ | 5 | - | nS |
| $e^{leak}$ | -60.6 | - | mV |
| $k^{AMPA}$ | $2^8$ | - | - |
| $k^{NMDA}$ | $2^{12}$ | - | - |
| $k^{GABA}$ | $2^8$ | $2^7$ | - |
| $k^{ext}$ | 5 | 1 | - |

Izhikevich Parameter values as in (Ferguson et al., 2014, 2013). Synaptic time constants: (Bartos et al., 2002; Geiger et al., 1997; Roth and van Rossum, 2009). Remaining parameters where adjusted to allow the network to generate a gamma rhythm.

**Figure supplements**

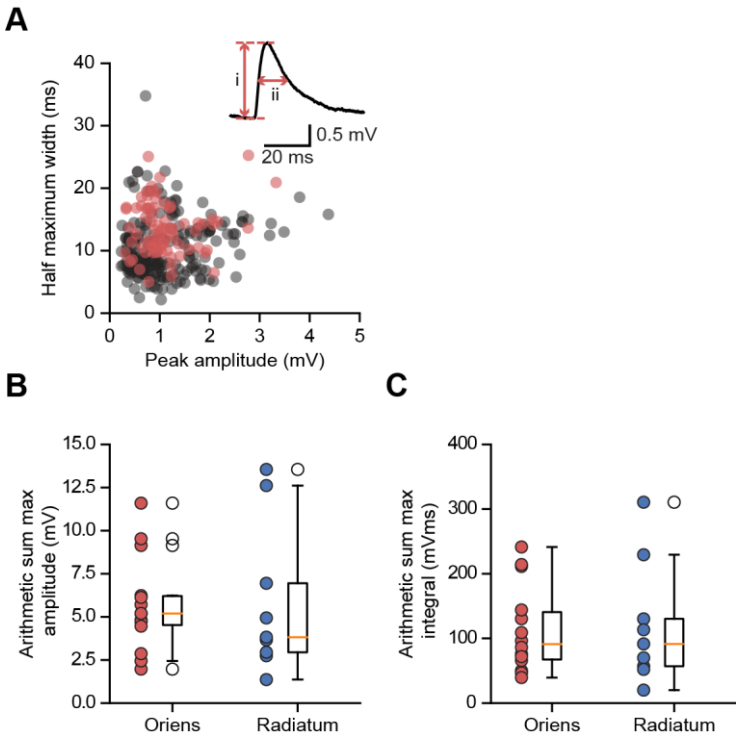


**Figure 1 – Figure Supplement 1.**
**Somatic glutamate uncaging-evoked membrane responses.**
(A) Comparison of uEPSPs to spontaneous EPSPs. Half-maximum width (ms) plotted against peak amplitude (mV) for n = 210 spontaneous events (gray) and n = 78 uEPSPs (red); data from 4 cells. Inset: peak amplitude (i) and half-width (ii) for one event.
(B) Distribution of arithmetic sum of peak amplitudes for oriens and radiatum uncaging locations.
(C) As (B) but for arithmetic sum of time-integrals.

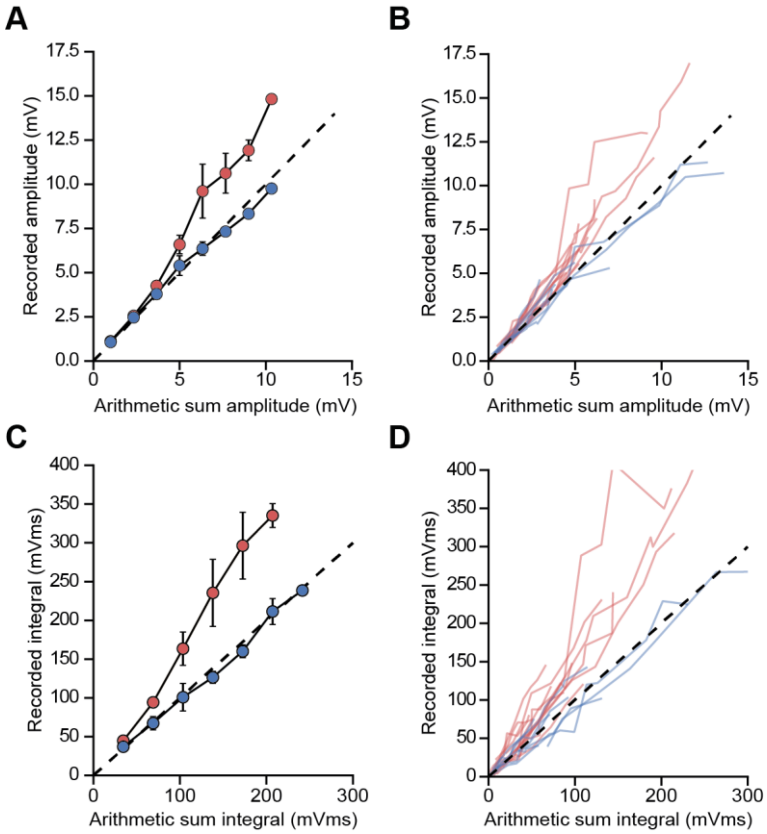


**Figure 1 – Figure Supplement 2.**
**Unscaled uEPSP integration location-dependent nonlinearity.**
Comparisons of the arithmetic sum of individual uEPSPs and corresponding recorded uEPSPs evoked at locations in stratum radiatum (blue, n = 9) and stratum oriens (red, n = 14).
(A, B) Unscaled uEPSP amplitudes, average (A) and raw data (B).
(C, D) Unscaled uEPSP integrals, average (C) and raw data (D).
For panels (A) and (C) linearly interpolated averages are shown ± SEM.

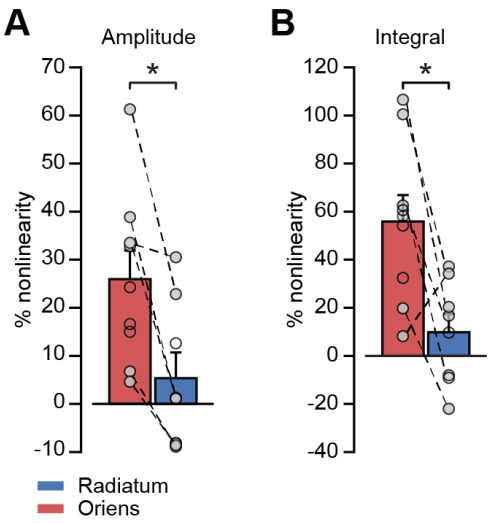


**Figure 1 – Figure Supplement 3.**
**uEPSP integration location-dependent nonlinearity by cell.**
(A) Peak amplitude nonlinearity comparison by dendrite location. Statistics for all data, oriens vs radiatum: 26.0 ± 6.0 % (n = 9) vs 5.4 ± 5.4 % (n = 8), *P* = 0.02. Statistics for paired data oriens vs radiatum: 29.6 ± 8.7 % vs 6.4 ± 6.7 %, *P* = 0.01, n = 6.
(B) Time-integral nonlinearity comparison by dendrite location. Statistics for all data, oriens vs radiatum: 55.9 ± 11.0 % (n = 9) vs 9.9 ± 7.6 % (n = 8), *P* = 0.004. Statistics for paired data, oriens vs radiatum: 59.3 ± 16.4 % vs 13.1 ± 9.6 %, *P* = 0.035, n = 6. Closed circles: paired recordings, open circles: unpaired. Bars show mean ± SEM of all recordings.

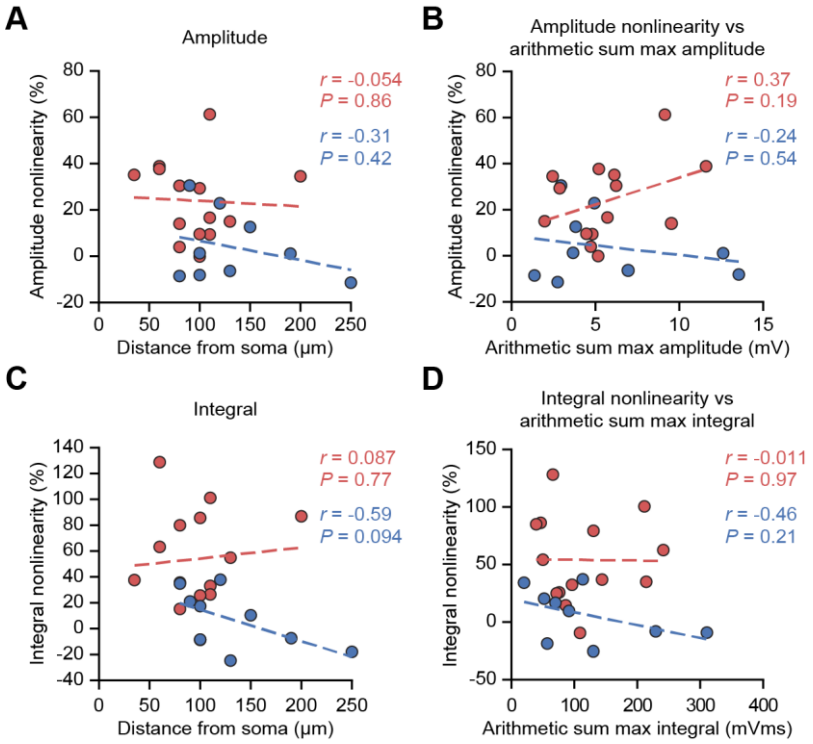


**Figure 1 – Figure Supplement 4.**
**uEPSP nonlinearity does not depend on uncaging location distance from soma or on the size of the arithmetic sum of uEPSPs.**
(A) uEPSP amplitude nonlinearity plotted against glutamate uncaging site distance from soma.
(B) uEPSP amplitude nonlinearity plotted against maximal arithmetic sum of uEPSP amplitudes.
(C) As (A) but for time-integrals.
(D) As (B) but for time-integrals.
Statistics: *r* = Pearson correlation coefficient, *P* = associated two-tailed significance.

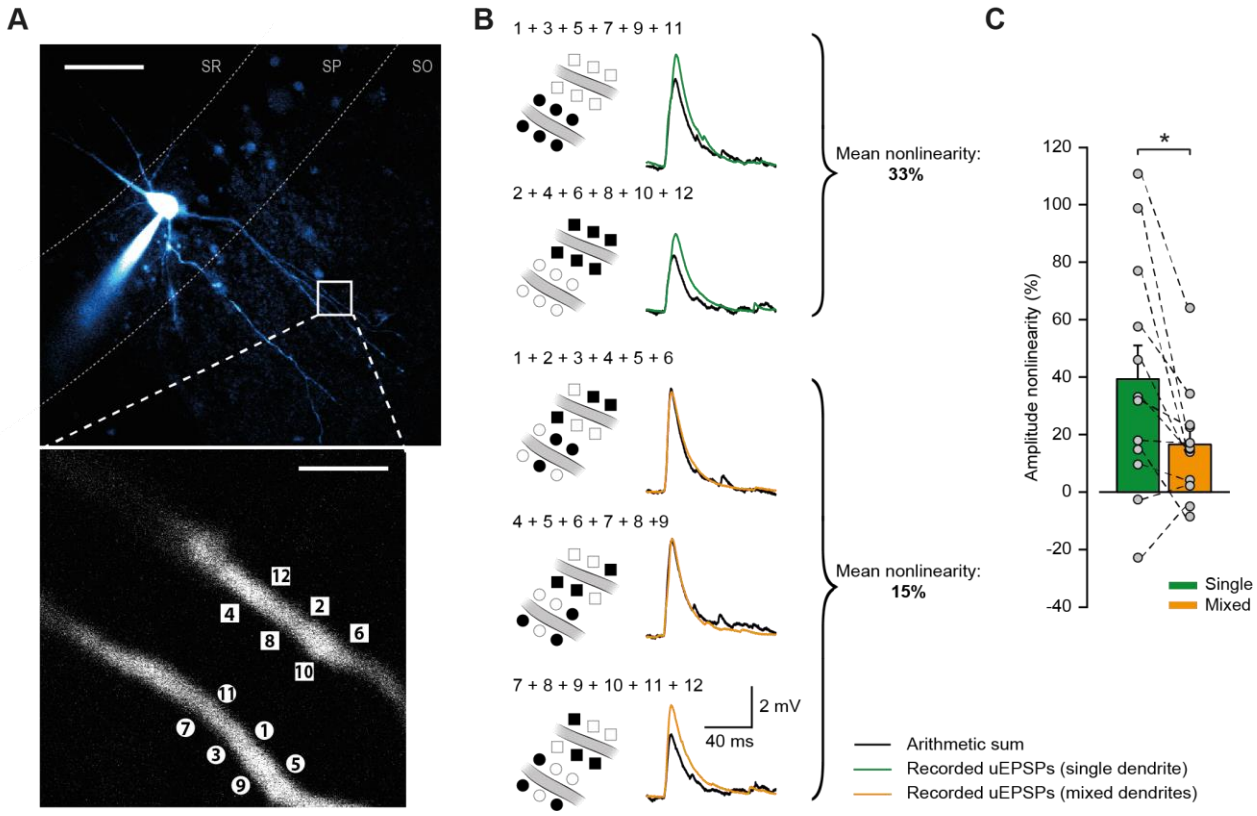


**Figure 1 – Figure Supplement 5.**
**Compound uEPSPs from uncaging locations clustered on a single dendrite display larger nonlinearities than when distributed across two dendrites.**
(A) Top: Two-photon z-stack of PV+ interneuron in CA1 region of hippocampus. White box marks region of interest shown below. Scale bar: 50 µm. Bottom: dendritic regions of interest at higher magnification showing glutamate uncaging locations (numbered) on two dendrites in the same focal plane. Scale bar: 3 µm.
(B) Comparison of arithmetic sum of six individual uEPSPs (black) and the recorded compound uEPSP elicited by uncaging glutamate on single dendrites (green) or across the two dendrites (orange).
(C) Summary of single- vs mixed-dendrite peak amplitude nonlinearity for all recordings. Statistics: paired t-test, single vs mixed nonlinearity: 39.3 ± 11.7 % vs 16.5 ± 5.6 %, $P$ = 0.016, n = 12 dendrite pairs, n = 6 cells. Error bars indicate mean ± SEM.

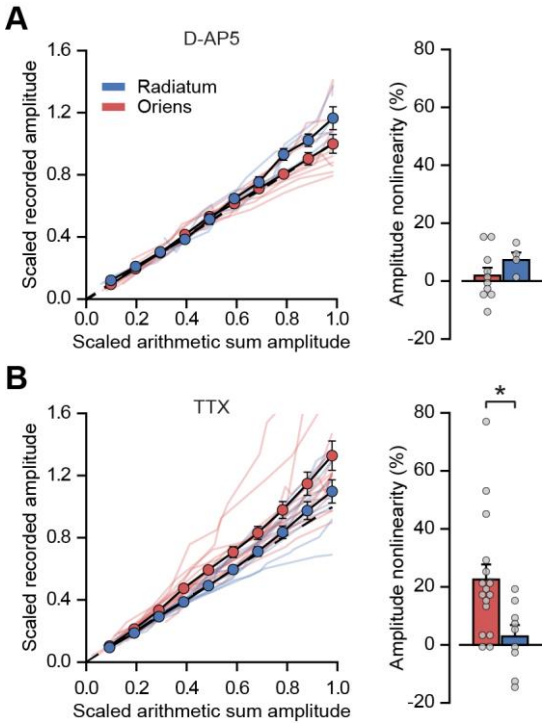


**Figure 2 – Figure Supplement 1.**
**Peak amplitude nonlinearity in oriens dendrites is abolished by blocking NMDARs with D-AP5 but not by blocking sodium channels with TTX.**
(A) Summary scaled peak amplitude uEPSP data for 14 dendritic locations recorded in D-AP5, n = 10 oriens; n = 4 radiatum. Right: quantified synaptic integration nonlinearity. Oriens vs radiatum: 1.9 ± 2.7 % vs 7.3 ± 2.5 %, $P$ = 0.27. Oriens D-AP5 vs oriens control, $P$ = 0.001. Radiatum D-AP5 vs radiatum control, $P$ = 0.66.
(B) Summary scaled peak amplitude uEPSP data for 25 dendritic locations recorded with TTX in the ACSF, n = 16 oriens; n = 9 radiatum. Right: quantified synaptic integration nonlinearity. Oriens vs radiatum: 22.6 ± 5.2% vs 2.9 ± 3.9%, $P$ = 0.016. Oriens TTX vs oriens control, $P$ = 0.84. Radiatum TTX vs radiatum control, $P$ = 0.9.

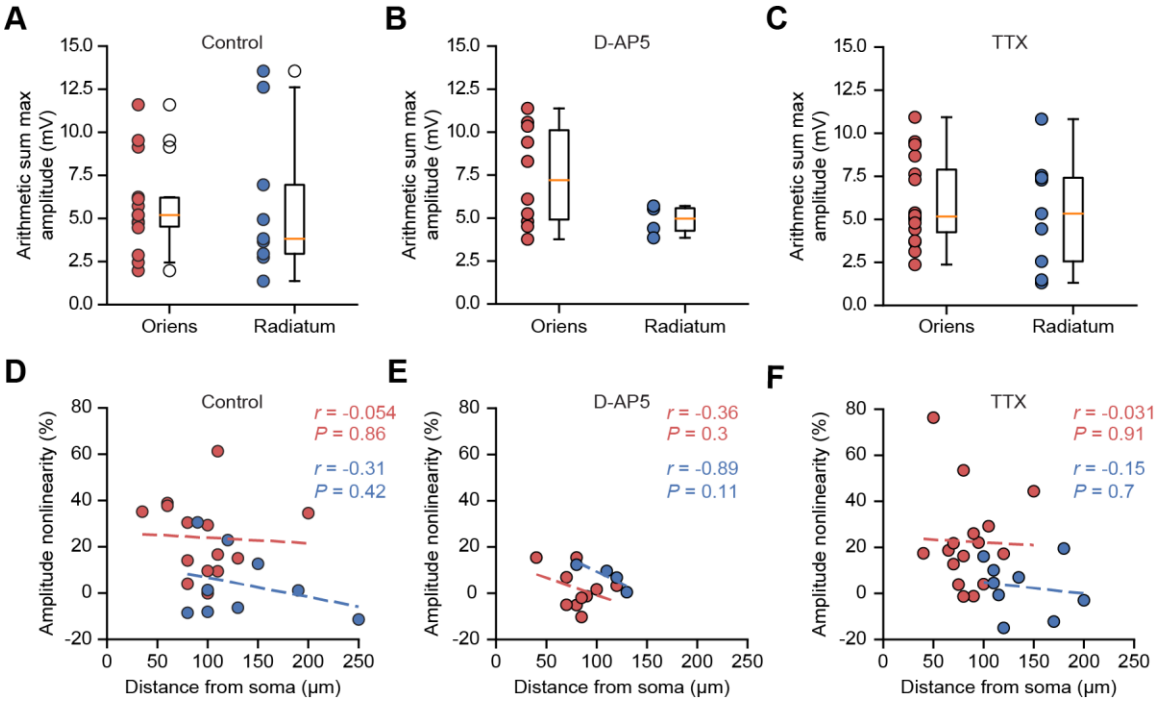


**Figure 2 – Figure Supplement 2.**
**Arithmetic sum maximum uEPSP amplitudes, and integration nonlinearity vs uncaging location distances, across pharmacological conditions.**
(A – C) Peak arithmetic uEPSP amplitudes by uncaging dendrite location in control conditions (A, replotted from Figure 1 – Figure Supplement 1B for comparison), D-AP5 (B), and TTX (C).
(D – F) uEPSP peak amplitude nonlinearity vs uncaging location distance from soma in control conditions (D, replotted from Figure 1 – Figure Supplement 4 for comparison), D-AP5 (E), and TTX (F).

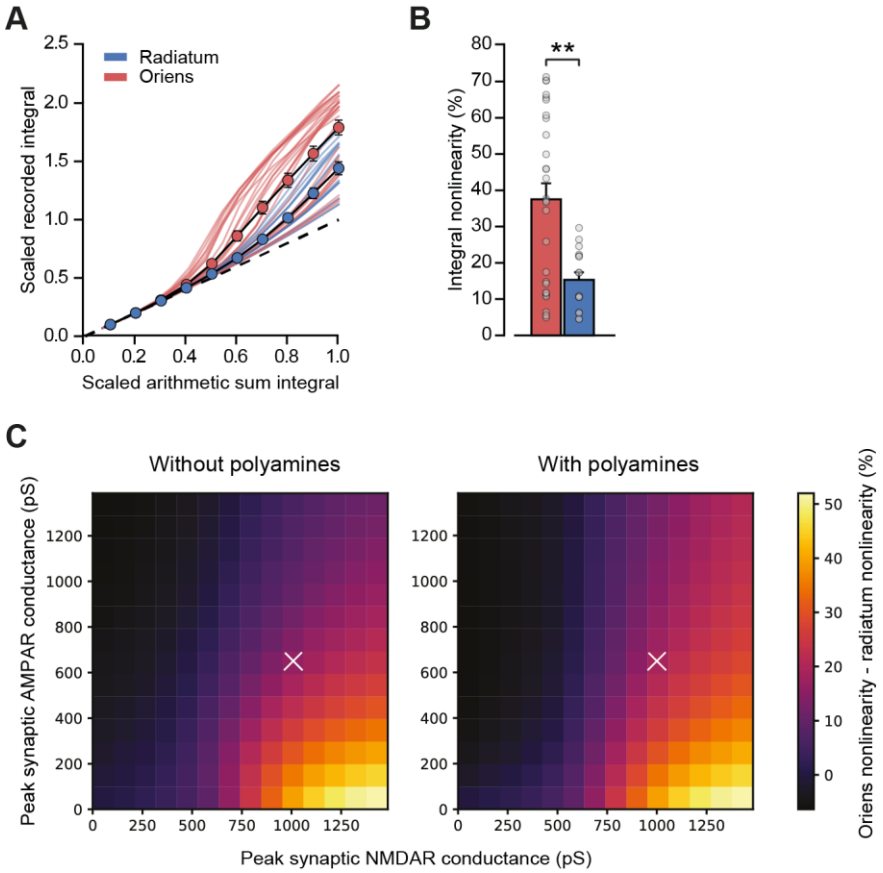


**Figure 3 – Figure Supplement 1.**
**Simulations including polyamine modulation of AMPARs show synaptic integration differences between strata oriens and radiatum dendrite locations.**
(A) Scaled recorded time-integrals vs scaled arithmetic sum of time-integrals at all locations with equal NMDAR conductance (oriens locations: n=28, radiatum locations: n=16). As Figure 3D, but with 100 µM intracellular spermine.
(B) Quantified synaptic integration nonlinearity, oriens 37.5 ± 4.4 % vs radiatum 15.3 ± 2.0.
(C) Mean percentage integral nonlinearity difference between oriens and radiatum dendrites as peak synaptic AMPA and NMDA receptor conductance is varied. White crosses denote parameter values for simulations shown in panel A and Figure 3D. Mean difference between simulations over parameter range was 2.77 ± 0.17 %. Polyamine modulation was simulated using a kinetic scheme based on (Bowie et al., 1998). Values for peak synaptic conductance were calculated at -60 mV and +60 mV for AMPA and NMDA receptors respectively. n=16 radiatum, n=28 oriens.

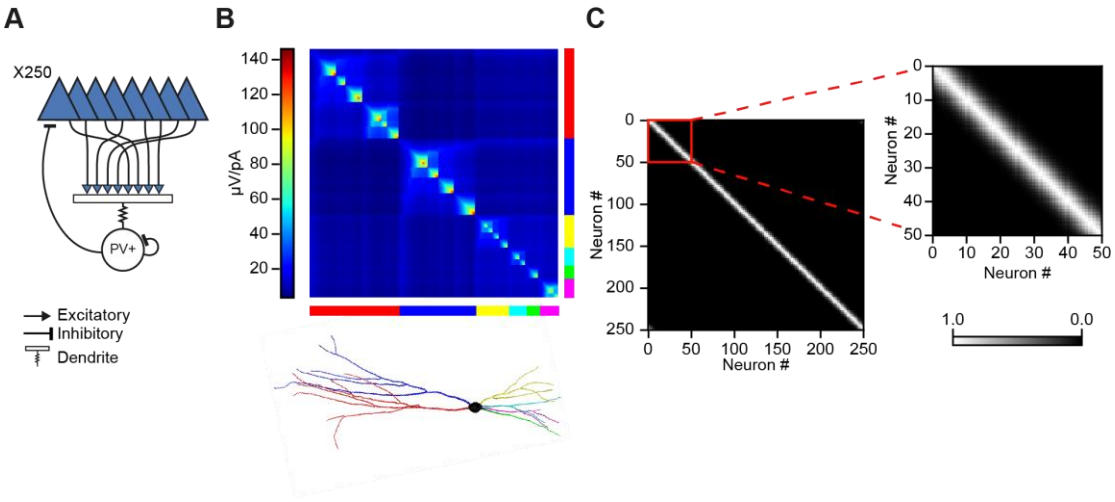


**Figure 5 – Figure Supplement 1.**

**Modelling principal cell input cooperation onto feedback interneurons.** (A) Network schematic showing postsynaptic membrane locations of Izhikevich-model PV+ interneuron.

(B) Steady state transfer resistance for a PV+ cell dendritic tree reconstructed using the TREES toolbox (Cuntz et al., 2010b). The matrix shows the electrotonic 'proximity' of neighbouring patches of membrane on the dendritic tree (color scale: µV/pA). The main branches of the dendritic tree are indicated at the bottom.

(C) Input cooperativity matrix used in simulations. Inset shows zoomed view of cooperativity matrix for the first 50 principal neurons.

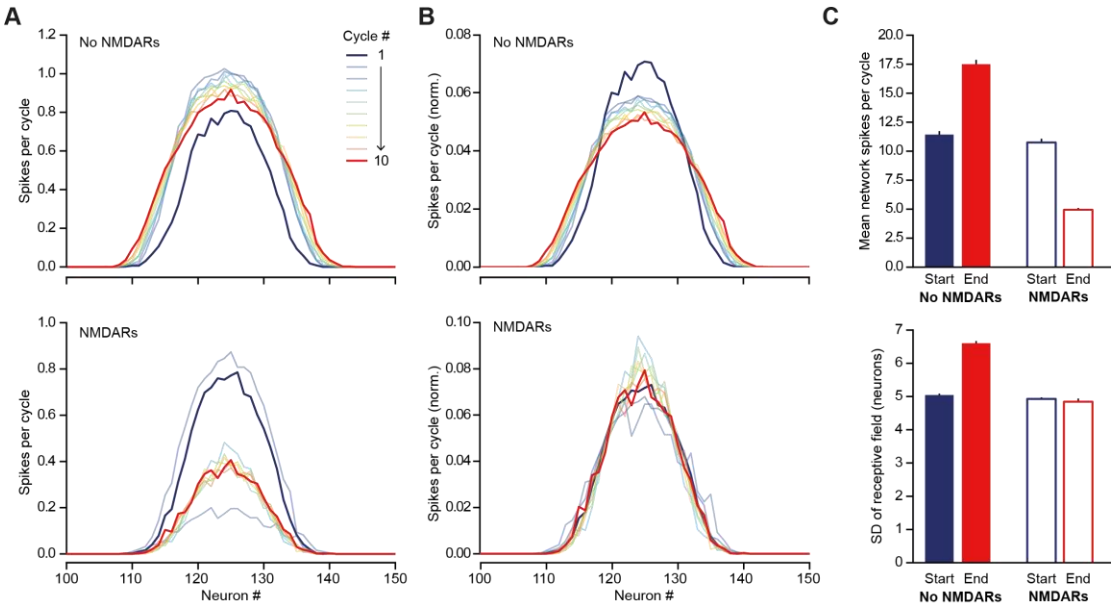


**Figure 5 – Figure Supplement 2.**
**NMDARs help to maintain a sparse and sharp representation of a 'hump' of excitation to the feedback circuit shown in Figures 5D.**
(A) Distribution of firing rate by neuron during each PV+ interneuron firing cycle, averaged across 500 simulations. Top – without NMDARs, bottom – with NMDARs. The hump of excitation was centred on neuron #125. Note the similarity of the first cycle between the two conditions. The behaviors of the networks diverge as the NMDARs are engaged.
(B) As (A) but normalized by total firing rates across neurons, for better comparison of distribution dispersion.
(C) Comparison of first and tenth simulation cycle: top – mean spikes per cycle, bottom - standard deviation of average network 'receptive field'.

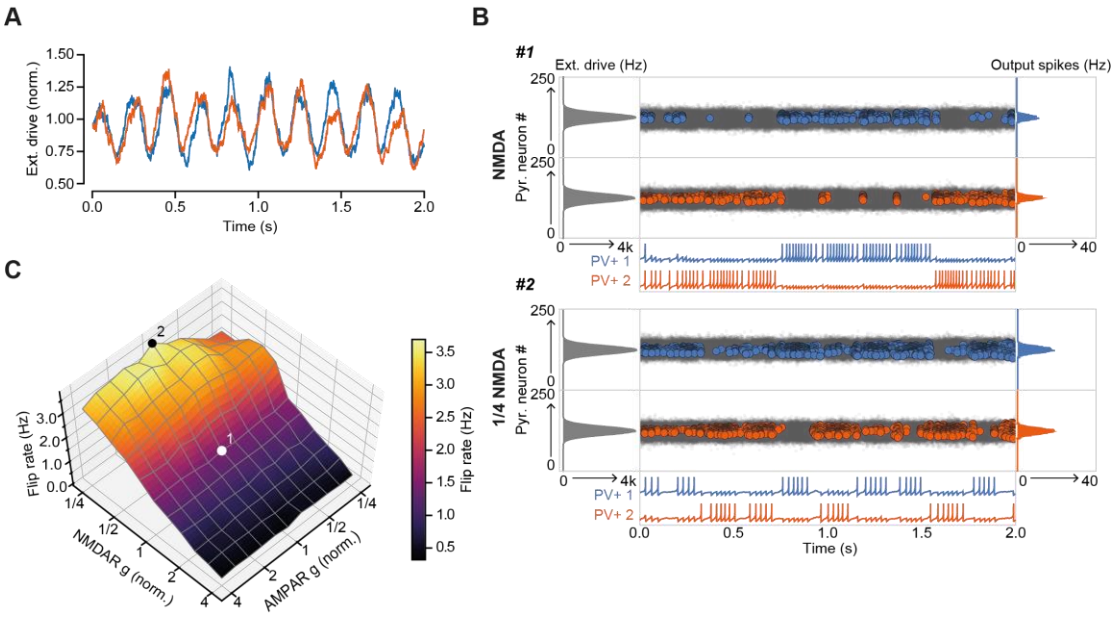


**Figure 7 – Figure Supplement 1.**
**The role of NMDARs at feedback connections in cell assembly stability with theta-modulated external drive.**
(A) Theta-modulated external drive to the system.
(B) Example simulation of network with NMDARs at synapses on interneurons (top), and with NMDARs scaled down to 25% of baseline (bottom). External drive (modulated as shown in panel A): gray; pyramidal cell firing: blue/orange, circles; interneuron firing: blue/orange spikes. Although the dominant networks flipped spontaneously in both cases, the frequency of flipping was much higher with the down-scaled NMDARs
(C) Plot of network flip rate vs NMDAR and AMPAR conductance. White point (1): baseline NMDAR simulation parameters; black point (2): NMDARs down-scaled to 25%.